Smoothened and ARL13B are critical in mouse for superior cerebellar peduncle targeting

Sarah K. Suciu[*,†,‡] Alyssa B. Long[†,‡] and Tamara Caspary[†]

[*]Genetics and Molecular Biology Graduate Program, [†]Department of Human Genetics, Emory University, Atlanta, GA 30322, [‡]These authors contributed equally

ORCID ID:

Suciu: 0000-0002-2416-9519

Long: 0000-0002-4467-4213

Caspary: 0000-0002-6579-7589

Summary statement

Joubert syndrome is diagnosed by the hindbrain "molar tooth sign" malformation. Using mouse models, we show loss of the ciliary GTPase ARL13B, mutations in which lead to Joubert syndrome, result in two features of the molar tooth sign: hypoplasia of the cerebellar vermis and inappropriate targeting of the superior cerebellar peduncles. Furthermore, we demonstrate that loss of vertebrate Hedgehog signaling may be the underlying disrupted mechanism as we extend its role in axon guidance to the superior cerebellar peduncles.

Running title (~35 characters, including spaces):

SMO and ARL13B in SCP targeting

Key words/phrases (up to ten):

molar tooth sign, Joubert syndrome, Smo, ARL13B, SCP targeting, cerebellar vermis

Corresponding author:

Tamara Caspary

Department of Human Genetics

615 Michael Street, Suite 301

Atlanta, GA 30322

404-727-9862

tcaspar@emory.edu

Abstract

Patients with the ciliopathy Joubert syndrome present with physical anomalies, intellectual disability, and a hindbrain malformation described as the “molar tooth sign” due to its appearance on an MRI. This radiological abnormality results from a combination of hypoplasia of the cerebellar vermis and inappropriate targeting of the white matter tracts of the superior cerebellar peduncles. ARL13B is a cilia-enriched regulatory GTPase established to regulate cell fate, cell proliferation and axon guidance through vertebrate Hedgehog signaling. In patients, mutations in *ARL13B* cause Joubert syndrome. In order to understand the etiology of the molar tooth sign, we used mouse models to investigate the role of ARL13B during cerebellar development. We found ARL13B regulates superior cerebellar peduncle targeting and these fiber tracts require Hedgehog signaling for proper guidance. However, in mouse the Joubert-causing R79Q mutation in ARL13B does not disrupt Hedgehog signaling nor does it impact tract targeting. We found a small cerebellar vermis in mice lacking ARL13B function but no cerebellar vermis hypoplasia in mice expressing the Joubert-causing R79Q mutation. Additionally, mice expressing a cilia-excluded variant of ARL13B that transduces Hedgehog normally, showed normal tract targeting and vermis width. Taken together, our data indicate that ARL13B is critical for control of cerebellar vermis width as well as superior cerebellar peduncle axon guidance, likely via Hedgehog signaling. Thus, our work highlights the complexity of ARL13B in molar tooth sign etiology.

INTRODUCTION

Joubert Syndrome and Related Disorders (JSRD) are recessive congenital disorders with a variety of symptoms including developmental delay, intellectual disability, abnormal respiratory rhythms, ataxia, oculomotor apraxia, polydactyly, craniofacial defects, retinal dystrophy, nephronophthisis, and hepatic fibrosis (Parisi *et al.* 2007, Bachmann-Gagescu *et al*. 2020). While the exact prevalence of JSRD is not known, published statistics range from 1:80,000 to 1:100,000, but these may be underestimates as suggested by a recent study (Brancati *et al.* 2010, Nuovo *et al.* 2020). The characteristic neuroanatomical feature of JSRD is the molar tooth sign (MTS), which is caused by hypoplasia of the cerebellar vermis and thickened, elongated superior cerebellar peduncles (SCPs) that fail to decussate (Maria *et al.* 1997;Yachnis and Rorke 1999; Poretti *et al.* 2007). However, little is known about the mechanistic etiology of this hindbrain malformation. This is especially significant as several symptoms of JSRD arise from defects in the hindbrain: cerebellar dysfunction commonly causes ataxia and hypotonia, while some patients manifest life-threatening breathing problems (Parisi 2019).

To date, mutations in over 35 genes cause JSRD, and their associated proteins almost always localize to the primary cilium or the centrosome (Parisi 2019). Thus, JSRD is classified as a ciliopathy, a category of human disease stemming from ciliary dysfunction. One of the genes implicated in JSRD is *ARL13B*, which encodes a regulatory GTPase highly enriched in cilia (Cantagrel *et al.* 2008; Bachmann-Gagescu *et al.* 2015; Thomas *et al.* 2015; Shaheen *et al.* 2016; Rafiullah *et al.* 2017). As a GTPase, ARL13B is expected to have multiple effector proteins which interact with

44 specific ARL13B residues. ARL13B can function as a guanine exchange factor (GEF)
45 for ARL3, mutations in which also lead to JSRD (Gotthardt *et al.* 2015; Ivanova *et al.*
46 2017). JSRD-causing mutations in either ARL3 or ARL13B can disrupt their interaction
47 or ARL13B's GEF activity, consistent with the notion that specific ARL13B function is
48 affected by JS-causing point mutations (Gotthardt *et al.* 2015; Ivanova *et al.* 2017;
49 Alkanderi *et al.* 2018). Most JSRD-causing ARL13B mutations cluster within the
50 protein's GTPase domain, although two are located in the coiled coil domains in the C
51 terminal half of the protein (Cantagrel *et al.* 2008; Bachmann-Gagescu *et al.* 2015;
52 Thomas *et al.* 2015; Shaheen *et al.* 2016; Rafiullah *et al.* 2017). ARL13B complexes
53 with the inositol phosphatase INPP5E, which is also implicated in causing JSRD (Bielas
54 *et al.* 2009; Humbert *et al*. 2012). ARL13B is critical for targeting INPP5E to cilia and
55 JSRD-causing ARL13B mutations disrupt INPP5E ciliary targeting (Humbert *et al.*
56 2012). INPP5E controls ciliary lipid composition through its phosphatase activity and
57 most JSRD-causing mutations are within its phosphatase domain (Bielas *et al.* 2009;
58 Chavez *et al.* 2015; Garcia-Gonzalo *et al.* 2015). Other proteins implicated in JSRD also
59 affect ciliary targeting with many functioning at the transition zone, supporting the notion
60 that abnormal ciliary traffic leading to defective signaling underlies JSRD (Arts *et al.*
61 2007; Delous *et al.* 2007; Garcia-Gonzalo *et al.* 2011; Hopp *et al.* 2011; Srour *et al.*
62 2012; Roberson *et al.* 2015).
63 The mechanistic connection between the cilia-related proteins implicated in
64 JSRD and the MTS are elusive in part because distinct biological processes are at play.
65 Abnormal proliferation may underlie the hypoplastic cerebellar vermis whereas defective
66 axonal targeting is likely involved in the abnormal SCP tracts. One signaling pathway

67 potentially linked to both processes is vertebrate Hedgehog (Hh) which relies on cilia
68 (Huangfu *et al.* 2003). Sonic hedgehog (Shh) is a mitogenic cue that controls
69 proliferation in the developing cerebellum so its misregulation could underlie the
70 cerebellar hypoplasia (Dahmane and Ruiz i Altaba 1999; Wechsler-Reya and Scott
71 1999; Kenney and Rowitch 2000). While the SCP tracts that normally project from the
72 deep cerebellar nuclei to the contralateral thalamus are guided by unknown signals,
73 Shh is a known commissural axon guidance cue (Charron *et al.* 2003). JSRD patients
74 can also display axon guidance defects in decussation of the pyramidal tracts (Yachnis
75 and Rorke 1999; Poretti *et al.* 1997).

76 *ARL13B* and *INPP5E,* encoding ciliary proteins linked to JSRD, are known to
77 regulate vertebrate Hh signaling. In mouse models, ARL13B loss disrupts cell fate
78 specification in the neural tube, proliferation of the cerebellar granule precursor cells in
79 the cerebellum and Shh-directed guidance of commissural axons in the spinal cord
80 (Caspary *et al.* 2007; Bay *et al.* 2018; Ferent *et al.* 2019). These data support a model
81 whereby disruption of Shh signaling by ARL13B mutation could provide a single
82 mechanism underlying the MTS. This model is bolstered by the fact that additional
83 phenotypes exhibited by JSRD patients, such as craniofacial defects or polydactyly, can
84 arise from aberrant Hh signaling (Valente *et al.* 2008; Lan and Jiang 2009; Lipinski *et al.*
85 2010).

86 As attractive as a Hh-based model for JSRD may be, not all the data support that
87 JSRD phenotypes result from misregulation of Hh signaling. Some features of JSRD,
88 such as the renal and liver anomalies, are not clearly due to misregulation of Hh
89 signaling (Doherty 2009; Breslow *et al.* 2018). Additionally, of over 35 genes implicated

90 in JSRD, only 22 play some role in Hh pathway regulation (Davey *et al.* 2006; Reiter
91 and Skarnes 2006; Caspary *et al*. 2007; Vierkotten *et al*. 2007; Huang *et al.* 2009;
92 Weatherbee *et al*. 2009; Bimonte *et al.* 2011; Dowdle *et al.* 2011; Sang *et al.* 2011; Chih
93 *et al.* 2011; Christopher *et al.* 2012; Thomas *et al.* 2012; Abdelhamed *et al*. 2013; Hynes
94 *et al*. 2014; Wu *et al.* 2014; Chavez *et al*. 2015; Garcia-Gonzalo *et al*. 2015; Asadollahi
95 *et al.* 2018; Frikstad *et al*. 2019; Munoz-Estrada and Ferland 2019). Some of these links
96 are tenuous. For example, mouse *Arl3* mutants mislocalize the Hh transcription factor,
97 GLI3, in their cilia yet do not exhibit any of the phenotypes normally displayed by
98 mutants in the Hh pathway (Schrick *et al.* 2006, Lai *et al.* 2011; Schwarz *et al.* 2017).
99 Additional signaling pathways are linked to cilia including others known to be important
100 in cell proliferation and axon guidance. Loss of either of the JSRD-linked genes *Ahi1* or
101 *Cep290* in mouse leads to a small cerebellar vermis due to aberrant Wnt signaling
102 (Lancaster *et al.* 2011; Ramsbottom *et al.* 2020). Possible JSRD-causing mutations in
103 *Znf423* are associated with defects in Wnt, BMP and retinoic acid signaling (Hata *et al.*
104 2000, Huang *et al.* 2009, Casoni *et al.* 2020, Deshpande *et al.* 2020). Conditional *Arl13b*
105 or *Inpp5e* deletion in the SCPs results in their disorganization and thickening through
106 misregulation of ciliary PI3 kinase and AKT (Guo *et al.* 2019).
107 Ciliopathies are well established to be genetically complex. JSRD patients with
108 different ARL13B mutations can display distinct phenotypes, such as obesity in an
109 individual expressing ARL13B^{Y86C} and occipital encephalocele in a patient expressing
110 ARL13B^{R79Q} (Cantagrel *et al.* 2008; Thomas *et al.* 2015). This is further exemplified in
111 cases of related individuals carrying the same mutation but exhibiting different
112 phenotypes and even diagnoses. For example, JSRD-causing mutations in TMEM67

113 (R208X) and TMEM216 (R73H) can also cause the more severe disease Meckel
114 syndrome (Consugar *et al.* 2007; Otto *et al.* 2009; Valente *et al.* 2010). Understanding
115 the genetic modifiers and environmental contribution underlying the phenotypic variation
116 will be key to understanding disease etiology as will understanding when and how
117 relevant pathways interact. In mouse models of the JSRD- and Meckel Syndrome-linked
118 gene *Tmem67*, two phenotypic categories emerged: one with cerebellar malformations
119 resembling JSRD and another with more severe CNS defects reminiscent of Meckel
120 syndrome (Abdelhamed *et al.* 2013). The two categories correlated with whether cilia
121 were retained, with the severe Meckel-like phenotype observed in animals lacking cilia.
122 Furthermore, the two phenotypic groups impacted Hh and Wnt signaling differently,
123 pointing to both pathways being critical (Abdelhamed *et al.* 2019). Importantly, it is not
124 simply whether cilia are present, as another JSRD mouse model, *Talpid3*, lacks cilia yet
125 displays a JSRD-like small cerebellar vermis (Bashford and Subramanian 2019). Thus,
126 mouse models are incredibly informative yet point to the enormous complexity
127 underlying the MTS.
128 Here we investigate the role of ARL13B in relation to Hh signaling in two major
129 features of the MTS: targeting of the SCPs to the thalamus and hypoplasia of the
130 cerebellar vermis. We explore these processes using a series of mouse alleles through
131 which we first define the roles of Hh signaling and ARL13B in SCP projections.
132 Subsequently, we untangle the role of ARL13B from within and outside of the cilium and
133 investigate a JS-causing patient allele. Taken together, our data illuminate the roles of
134 ARL13B in MTS etiology and the complexity in modeling aspects of the MTS in mouse.
135

136 **MATERIALS & METHODS**

137 *Mouse lines*

138 All mice were cared for in accordance with NIH guidelines and Emory
139 University's Institutional Animal Care and Use Committee (IACUC). Lines used were
140 *Nex-Cre* (C3H-HeJ-*Neurod6*$^{tm1(cre)Kan}$) [MGI:2668659], *Brn4-Cre* (C3H/HeJ-*Tg(Pou3f4-*
141 *cre)32Cren*) [MGI:2158470], *Smo*^{flox} (C3H/HeJ-*Smo*^{tm2AMC}) [MGI:2176256], *Arl13b*^{flox}
142 (C3H/HeJ-*Arl13b*^{tm1Tc}) [MGI:4948239], *Arl13b*^{V358A} (C57BL/6J-*Arl13b*^{em1Tc})
143 [MGI:6256969], and *Arl13b*^{R79Q} (C57BL/6J-*Arl13b*^{em2Tc}) [MGI:6279301]. Note that
144 *Arl13b*$^{\Delta}$ is the deletion allele resulting from germline deletion of the conditional *Arl13b*^{flox}
145 allele. Genotyping was as previously described (Heydemann *et al.* 2001; Goebbels *et*
146 *al.* 2006; Nolan-Stevaux *et al.* 2009; Su *et al.* 2012; Gigante *et al.* 2020).

147 To generate the R79Q mutation in *Arl13b*, a CRISPR gRNA
148 (ATTATTATGCTGAATCCTA*TGG*; PAM sequence is italicized) targeting exon 3 of the
149 *Arl13b* locus along with a 180bp donor oligo (5'-CTCCCACTGTTGGCTTTTCTAAAA-
150 TTGATCTGAGACAAGGAAAGTTCCAAGTTACCATCTTTGACTTAGGAGGTGGAAAA
151 AGAATTCAGGGCATATGGAAGAATTATTATGCTGAATCCTATGGGGTAATATTTGTT
152 GTGGATTCCAGTGATGAGGAGAGAATGGAAGAAACAAAGGAGA-3'; underlined
153 bases are engineered) were designed to generate a G-to-A change creating the R79Q
154 point mutation as well as A-to-C and T-to-A silent changes to create a *Nde*I restriction
155 site that could be used for genotyping (Millipore Sigma). The gRNA (50 ng/ul), ssDNA
156 oligo donor (50 ng/ul) and wild type *Cas9* mRNA (10 ng/ul) were injected into 1-cell
157 C57BL/6J zygotes and subsequently transplanted at the 2-cell stage into C57BL/6J
158 pseudopregnant females by the Emory Transgenic and Gene Targeting Core; all

159 reagents were purchased from Millipore Sigma. Genomic DNA from toes was amplified
160 via PCR using primers (5'-TCACTTGCAACAGAGCATCC-3') and (5'-
161 ACAGCTCTGCCCGTGTTTAC-3') located upstream and downstream of the donor oligo
162 breakpoints; products were sequenced with the forward (first) primer. A single founder
163 animal heterozygous for both the R79Q mutation and NdeI restriction site was identified
164 with no additional editing. Subsequent allele-specific genotyping of progeny was
165 performed on ear punch or yolk sac using the following primers: Fwd-wt primer: 5'-
166 GGAGGTGGAAAAAGAATaCg-3'; Fwd-mut primer: 5'-
167 gctctatggctgGGAGGTGGAAAAAGAATTga-3'; Rev primer: 5'-
168 AGTGCTAAGACACCCGAGGA-3'. PCR bands at 142bp (wild type) and/or 154bp
169 (mutant) were produced, due to the addition of 12 non-templated bases to the 5' end of
170 the Fwd-mut primer (lowercase). Note the 3' ends of the two forward primers differed in
171 the base that codes for the R to Q change (final nucleotide of the primer) and includes a
172 "wobble" base (lowercase) to provide allele-specific amplification after the first round of
173 PCR (Gaudet *et al.* 2009). In order to breed away any potential off-target edits, the
174 founder was backcrossed to C57BL/6J for three generations with at least two
175 independent meiotic opportunities for recombination in each generation.
176
177 *Tract tracing injections and analysis*
178 Tract tracing experiments were performed according to a protocol approved by
179 Emory University's Institutional Animal Care and Use Committee (IACUC). Male and
180 female mice at postnatal day 90 or older were used for tract tracing experiments. At
181 least 3 mice of each genotypic group were analyzed in experiments (exact N included in

182 Figures 1-3, S1). Mice were anesthetized with inhaled isoflurane and maintained under
183 anesthesia throughout the procedure. Animals were secured in the stereotax, and the
184 scalp was opened with bregma and lambda aligned to flatskull position. Dorsal thalamus
185 injections were targeted to the bregma (AP:-0.70, ML:+1.13, DV:-3.28, Angle:0°) and
186 ventral thalamus injections were targeted using coordinates to the bregma (AP:-0.70,
187 ML:-3.11, DV:-4.69, Angle:25°). Ventral injection targeting includes a 25° angle to avoid
188 pulling dye through the dorsal thalamus upon needle removal. Then, a 5 ul Hamilton
189 microsyringe was lowered to target and target was injected with lysine fixable dextran
190 tetramethylrhodamine neuroanatomical tracer (fluoro-Ruby, 10,000 MW, ThermoFisher
191 Scientific D1817). Animals received 0.05 - 0.5 ul injections of 10% dextran
192 tetramethylrhodamine in sterile phosphate buffered saline (PBS, pH = 7.25) unilaterally
193 at a rate of 0.1 ul/minute. The 0.5 ul injection volume initially used resulted in high
194 background (non-specific) fluorescence. Later surgeries were conducted with 0.05 ul of
195 dye, which resulted in lower background and retention of a strong signal in the DCN.
196 Seven days post-procedure, mice were perfused with 50mls of PBS followed by
197 30mls of 4% paraformaldehyde (PFA). Brains were kept in PFA overnight and
198 subsequently placed in 30% sucrose in 0.1M phosphate buffer (pH 7.3) for
199 cryoprotection for at least 48 hours. Brains were embedded in Tissue-Tek OCT
200 compound (Sakura) for coronal cryostat sectioning. Sections were 60 microns thick and
201 processed through 70% ethanol dehydration and 0.1% sudan black autofluorescence
202 quencher, rehydrated in PBS and treated with DAPI to stain nuclei prior to fluorescence
203 imaging. Images were taken on a Lionheart FX automated microscope (Biotek) or at 5x
204 magnification on a Leica DM6000B microscope (Leica) using SimplePCI imaging

205 software (Hamamatsu). The Leica images were subsequently stitched together to reveal
206 the entirety of the brain section in Fiji (Schindelin *et al.* 2012) or Photoshop (Adobe).
207 Surgical injection sites were assessed to ensure dye was present at the desired
208 injection site. If the injection was off-target or dye at the injection site was not seen,
209 samples were removed from analysis. Cerebellar images from injections were evaluated
210 for DCN staining with assessor blinded to genotype. The number of injections that
211 resulted in fluorescent DCN for each injection site (dorsal and ventral thalamus) were
212 compared between mutant and control genotypes using a two-sided Fisher's exact test
213 (PRISM 8.2.0).
214
215 *Phenotypic analysis of embryos*
216 Timed matings of mice were performed to generate somite-matched embryos at
217 embryonic day 10.5 (E10.5). Embryos were dissected in cold PBS and processed for
218 immunofluorescence staining as previously described (Constable *et al.* 2020). Primary
219 antibodies used were: mouse anti-Shh (5E1, 1:10), mouse anti-Pax6 (PAX6, 1:100)
220 (Developmental Studies Hybridoma Bank), rabbit anti-Olig2 (AB9610, 1:500, Millipore
221 Sigma), and mouse anti-Arl13b (N295B/66, 1:1500, NeuroMab). Multiple sections from
222 three embryos of each genotype were examined.
223
224 *Analysis of anatomical measures*
225 Weanling age (P20-P24) male and female mice were sacrificed and brains were
226 harvested and fixed in 4% PFA overnight at 4º. Ten sex-matched pairs of mouse brains
227 were collected for each genotype; control animals were either wild type or heterozygous

228 for the *Arl13b* point mutation or floxed allele (so *Arl13b*$^{R79Q/+}$, *Arl13b*$^{V358A/+}$ or *Arl13b*$^{flox/+}$)
229 or lacked *Brn4-Cre* (for *Arl13b*$^{Brn4\text{-}Cre}$). Brains were imaged on a tilted stage to present a
230 surface view of the cerebellum, with a standard ruler in frame to confirm scale, using a
231 dissecting microscope (Leica MZFLIII). Measurements were made in FIJI (Schindelin *et*
232 *al.* 2012) with the investigator blind to genotype. Whole cerebellar width was measured
233 at the widest part of the cerebellum, coinciding with lobule CI or CII. Vermis width was
234 calculated by measuring the widest part of lobule VII (Deshpande *et al.* 2020).
235 Hemisphere and vermis heights were measured at the longest rostro-caudal point of the
236 hemisphere or at the midline of the vermis (see Figure 5). Body and brain weights were
237 measured on a standard lab scale. For each sex- and age-matched pair, the ratio of
238 mutant to control measures were calculated and graphed. A one-sample t-test was
239 performed after transforming the ratio data to a log(2) scale to normalize data
240 distribution (PRISM 8.2.0). Using the vermis width measures from our control brains
241 (mean = 2.6mm, SD = 0.18), a power calculation for a one-sided t-test estimated 90%
242 power to detect a 10% difference with 9-10 paired samples for a nominal alpha=0.05
243 (https://clincalc.com/stats/samplesize.aspx and
244 https://www.stat.ubc.ca/~rollin/stats/ssize/n2.html).
245

246 ***Data availability***

247 Mouse lines are available upon request. Supplemental material available at
248 figshare. Figure S1 contains diagrams illustrating the complete results of the injection
249 and tract tracing experiments. Figure S2 contains a schematic of the CRISPR strategy.

250 The authors affirm that all data necessary for confirming the conclusions of the article
251 are present within the article and figures.
252
253 **RESULTS**
254 *SMO is required for normal SCP projection to the dorsal thalamus*
255 In order to test whether proper projection of SCPs requires Hh signaling, we
256 compared the SCP tracts in mice in which we deleted the gene encoding the obligate
257 Hh transducer, *Smoothened* (*Smo*), to control animals. As *Smo* null embryos die during
258 embryogenesis, we deleted *Smo* specifically in the projection neurons by generating
259 *Nex-Cre;Smo*$^{fl/fl}$ mice, which we refer to as *Smo*$^{Nex\text{-}Cre}$ (Zhang *et al.* 2001; Caspary *et al.*
260 2002). *Nex-Cre* initiates CRE recombinase expression at E11.5, as the precursor cells
261 of the deep cerebellar nuclei (DCN) begin to migrate and become specified (Fink *et al.*
262 2006; Goebbels *et al.* 2006). In the mature cerebellum, the SCPs project rostrally from
263 the DCN (illustrated in Figure 1A). After entering the midbrain, the SCPs cross the
264 midline and again turn rostrally to project to two positions in the rostral thalamus: one
265 tract takes a slight dorsal path and the other tract remains in the same plane; for
266 simplicity here, we term these projection sites the dorsal and ventral thalamus,
267 respectively (Bohne *et al.* 2019). To examine the SCP tracts, we used retrograde tract
268 tracing in which we performed stereotaxic injections of a lipophilic dextran dye into
269 either the dorsal (Figure 1B) or ventral (Figure 1C) thalamus and allowed the dye to
270 diffuse through the axons to the associated neuron's cell body (~7 days); we then
271 sacrificed the animal and examined the cerebellum for evidence of the lipophilic dye
272 indicating tracing.

273 We found that both dorsal and ventral thalamus injections resulted in visible
274 clusters of dye-stained cells in the contralateral DCN, and not the ipsilateral DCN, in
275 control animals indicating the retrograde tract tracing reliably labelled the SCPs in our
276 hands (Figures 1D-E, S1A-B, dorsal: 6/8; ventral: 8/11). In the *Smo*$^{Nex\text{-}Cre}$ mice, the
277 results differed depending on whether we injected in the dorsal or ventral thalamus
278 (Figures 1F-G, S1C-D). In the ventral thalamus injections, we detected dye-stained
279 clusters of cells in the contralateral DCN but not the ipsilateral DCN, indicating normal
280 SCP projection to the ventral thalamus (Figure 1G, 4/4 injections). This indicates that at
281 least some SCPs cross the midline. In the dorsal thalamus injections, we could not
282 detect dye-stained clusters of cells in either the contralateral or ipsilateral DCN (Figure
283 1F, 0/6 injections) suggesting that SCPs lacking SMO do not project to the dorsal
284 thalamus. These data implicate SMO as critical for proper projection of the SCPs to the
285 dorsal thalamus.
286
287 *ARL13B is required for normal SCP projection to the dorsal thalamus*
288 Given that ARL13B regulates vertebrate Hh signaling in a variety of contexts, we
289 next assessed ARL13B's role in proper SCP projection. In order to delete *ARL13B*
290 specifically in projection neurons, we generated *Nex-Cre;Arl13b*$^{fl/fl}$ mice, which we refer
291 to as *Arl13b*$^{Nex\text{-}Cre}$*.* We performed dorsal and ventral thalamus injections for retrograde
292 tract tracing to examine the SCPs (Figures 1H-I, S1C-D). In the ventral thalamus
293 injections of *Arl13b*$^{Nex\text{-}Cre}$ mice, we found dye-stained clusters of cells in the
294 contralateral DCN consistent with normal SCP projections crossing the midline and
295 projecting to the ventral thalamus (Figure 1I, 4/4 injections). In contrast, in the dorsal

296 thalamus injections of *Arl13b*$^{Nex\text{-}Cre}$ mice, we generally did not detect dye-stained
297 clusters of cells in either the contralateral or ipsilateral DCN, suggesting that the SCPs
298 lacking ARL13B do not project to the dorsal thalamus (Figure 1H, 1/7 injections). These
299 data link ARL13B function to normal SCP projection. Furthermore, they reveal a similar
300 phenotype in *Smo*$^{Nex\text{-}Cre}$ and *Arl13b*$^{Nex\text{-}Cre}$ mice.
301
302 *ARL13B does not function from within cilia to mediate SCP guidance*
303 *ARL13B* and the other 35 genes implicated in Joubert syndrome associate with
304 the cilium or centrosome leading to the assumption that protein dysfunction from these
305 locales underlies JSRD phenotypes (Parisi 2019). To directly ask whether ARL13B
306 mediates SCP guidance to the dorsal thalamus from within cilia, we examined a mouse
307 expressing a cilia-excluded variant of ARL13B, ARL13B^{V358A} (Figure 2) (Gigante *et al.*
308 2020). We previously demonstrated that ARL13B^{V358A} retains all known ARL13B
309 biochemical activity, is undetectable in cilia yet transduces vertebrate Hh signaling
310 normally (Mariani *et al.* 2016; Gigante *et al.* 2020). We found that either dorsal or ventral
311 thalamus injections resulted in visible clusters of dye-stained cells in the contralateral
312 DCN in control (Figures 2A-B, S1G-H, dorsal: 3/3; ventral: 4/4) and *Arl13b*$^{V358A/V358A}$
313 (Figure 2C-D, dorsal: 4/4; ventral: 3/3) animals. In the context of the previous result
314 showing that *Arl13b*$^{Nex\text{-}Cre}$ mice display abnormal SCP projections to the dorsal
315 thalamus, these data demonstrate that ARL13B does not function from within cilia to
316 regulate SCP projections.
317
318 *SCP projection is normal in mice expressing a Joubert-causing allele*, Arl13b^{R79Q}

319 In order to understand the relationship between ARL13B and MTS formation in
320 Joubert syndrome, we generated a mouse expressing the JSRD-causing R79Q
321 mutation (Figure 3A). We used CRISPR/Cas9 editing to change the conserved residue
322 in the mouse genome (Figures 3B, S2). This amino acid change disrupts ARL13B's
323 GEF activity for ARL3 (Gotthardt *et al.* 2015; Ivanova *et al.* 2017). We found
324 *Arl13b*$^{R79Q/R79Q}$ mice were viable and fertile. We bred the *Arl13b*^{R79Q} allele to the null
325 *Arl13b*$^{\Delta}$ allele to make *Arl13b*$^{R79Q/\Delta}$ animals, which we found survived to adulthood. As
326 *Arl13b*$^{\Delta/\Delta}$ are embryonic lethal, this genetically demonstrates that *Arl13b*^{R79Q} is a
327 hypomorphic allele of *ARL13B* (Su *et al.* 2012).
328 To assess the role of ARL13B^{R79Q} in SCP guidance, we performed dorsal and
329 ventral thalamus dye injections in control and *Arl13b*$^{R79Q/R79Q}$ mice. We identified visible
330 clusters of dye-stained cells in the contralateral DCN in control (Figures 3C-D, S1E-F,
331 dorsal: 4/4; ventral: 3/3) and *Arl13b*$^{R79Q/R79Q}$ (Figure 3E-F, dorsal: 3/3; ventral: 3/4)
332 animals. Thus, despite the constitutive expression of the JSRD-causing allele
333 throughout development, we did not detect a SCP projection defect in the
334 *Arl13b*$^{R79Q/R79Q}$ mouse model. In the context of the abnormal SCP projections to the
335 dorsal thalamus that we identified in the *Smo*$^{Nex\text{-}Cre}$ and *Arl13b*$^{Nex\text{-}Cre}$ mice, this result
336 indicates that the *Arl13b*^{R79Q} allele does not disrupt SMO function or any ARL13B
337 function that regulates SMO.
338
339 *Arl13b*$^{R79Q/R79Q}$ *mice display normal Shh signal transduction in neural tube patterning*
340 To further investigate the role of the *Arl13b*^{R79Q} allele in Hh signaling, we
341 examined embryonic neural patterning as it is exquisitely sensitive to alterations in Shh

342 activity (Chiang *et al.* 1996; Briscoe and Ericson 1999). We generated E10.5 embryos
343 and stained neural tube sections with antibodies against Shh, Olig2 and Pax6 (Figure
344 4). As expected in wild type embryos, we observed Shh expression in the ventral-most
345 cells (the floorplate), Olig2 expression in lateral cells and Pax6 expression dorsally. We
346 also saw the established abnormal cell fates in null *Arl13b*$^{\Delta/\Delta}$ embryos: loss of Shh
347 staining in the floorplate (Figure 4D), dorsal and ventral expansion of Olig2 expression
348 (Figure 4H), and a dorsal shift in Pax6 expression (Figure 4L) (Su *et al.* 2012). We
349 found both *Arl13b*$^{R79Q/R79Q}$ (Figure 4B, F, J) and *Arl13b*$^{R79Q/\Delta}$ (Figure 4C, G, K) embryos
350 displayed neural patterning indistinguishable from wild type embryos, indicating the
351 *Arl13b*^{R79Q} allele is not dosage-sensitive and does not disrupt Shh signaling in
352 determining neural cell fate. In addition, ARL13B^{R79Q} protein localized to cilia (Figure
353 4N), consistent with previous results (Li *et al.* 2010; Humbert *et al.* 2012; Li *et al.* 2016;
354 Mariani *et al.* 2016).
355
356 *Arl13b*$^{R79Q/R79Q}$ *mice display normal cerebellar width*
357 The lack of a SCP projection phenotype in the *Arl13b*$^{R79Q/R79Q}$ mice surprised us
358 since JS patients display the MTS. In addition to defects in the SCPs, the MTS is due to
359 an underdeveloped cerebellar vermis, so we examined the width of the cerebellum and
360 the cerebellar vermis (Figure 5) (Aguilar *et al.* 2012). To quantify cerebellar width, we
361 performed analysis of surface-facing anatomical measurements validated to be
362 sufficiently sensitive to detect small differences in vermis width (Deshpande *et al.* 2020).
363 Briefly, we measured cerebellar width as well as cerebellar vermis width (widest part of
364 lobule VII) of fixed whole mount dissected brains. For each sex- and age-matched pair,

365 we calculated the ratio of the width measurements from mutant to control, which we
366 compared to a hypothetical value of 1 (indicating no difference between groups). We
367 detected no differences in the overall cerebellar width or the cerebellar vermis width
368 between control and *Arl13b*$^{R79Q/R79Q}$ mice of either sex (Figure 5B). Furthermore, we
369 found no difference in body or brain weight for *Arl13b*$^{R79Q/R79Q}$ mutants compared to
370 controls (Figure 5B). Thus, unlike patients carrying *ARL13B*$^{R79Q/R79Q}$, *Arl13b*$^{R79Q/R79Q}$
371 mice do not display a detectable growth deficit in the cerebellar vermis.
372
373 *Global cerebellar hypoplasia is observed in mice lacking Ar13b in all neurons*
374 Cerebellar size is well established to be regulated, in part, via Shh signaling
375 which controls proliferation of the cerebellar granule precursor cells (Kenney and
376 Rowitch 2000; Chizhikov *et al.* 2007). In order to better understand the vermis
377 hypoplasia phenotype seen in JBTS patients in relation to ARL13B, we wanted to
378 investigate how ARL13B regulates cerebellar width. To do so, we crossed the *Brn4-Cre*
379 allele into the conditional null *Arl13b*$^{fl/fl}$ background, called *Arl13b*$^{Brn4\text{-}Cre}$ (Figure 6). *Brn4-*
380 *Cre* initiates expression at E8.5 throughout the neuroectoderm so the cerebellum
381 develops in the absence of ARL13B (Heydemann *et al.* 2001; Hazen *et al.* 2012). We
382 again calculated width ratios using surface-facing anatomical measurements and found
383 the overall width of the cerebellum was 6% reduced in both females and males lacking
384 ARL13B compared to control littermates at weaning (Figure 6B, $p<0.1$). More striking, in
385 the cerebellar vermis we detected a 27% reduction in width in female and a 33%
386 reduction in male mutants compared to controls (Figure 6B, $p<0.0001$). *Arl13b*$^{Brn4\text{-}Cre}$
387 mice develop hydrocephaly just after weaning which often leads to death. This is

388 reflected in the body and brain weight ratios: while the mutant mice had slightly lower
389 body weights, they had comparatively heavier brains (Figure 6B). From these data, we
390 conclude that loss of *ARL13B* leads to a modest global cerebellar width deficit and a
391 more pronounced cerebellar vermis width reduction.
392
393 *Arl13b$^{V358A/V358A}$ mice display normal cerebellar width*
394 JS is classified as a ciliopathy due to the majority of causative genes encoding
395 proteins that, like ARL13B, are associated with cilia. In order to better understand the
396 role of ciliary ARL13B in cerebellar size, we examined cerebellar width in the mice
397 expressing the cilia-excluded variant ARL13B^{V358A} (Figure 7) (Gigante *et al.* 2020). We
398 detected no difference in the overall cerebellar width or that of the cerebellar vermis
399 between control and *Arl13b$^{V358A/V358A}$* mice (Figure 7B). Thus, ARL13B does not control
400 cerebellar width from within cilia.
401
402 **DISCUSSION**
403 Here we demonstrate that complete loss of *Arl13b* function in mouse can account
404 for two aspects of the MTS: aberrant SCP thalamic targeting and cerebellar vermis
405 hypoplasia. We expand the role of Hh signaling as a critical guidance cue by showing it
406 is required for proper SCP projection to the dorsal thalamus. Our finding that the SCP
407 phenotype is similar in *Smo$^{Nex\text{-}Cre}$* and *Arl13b$^{Nex\text{-}Cre}$* mice is consistent with a model
408 whereby ARL13B regulates SCP projections to the dorsal thalamus via a SMO-
409 dependent mechanism. In line with previous work showing that ARL13B does not
410 function from within cilia to regulate Shh-guided axon guidance, we found normal SCP

411 thalamic targeting in mice expressing only a cilia-excluded ARL13B variant (Ferent *et al.*
412 2019). By mutating a conserved arginine to glutamine, we generated a mouse
413 expressing a mutation linked to JSRD in humans and observed no change in vertebrate
414 Hh signaling (Cantagrel *et al.* 2008). Additionally, we identified no defects in
415 *Arl13b*$^{R79Q/R79Q}$ SCP projections. Whereas complete ARL13B deletion (*Arl13b*$^{Brn4\text{-}Cre}$) in
416 the cerebellum led to global hypoplasia, we show the cerebellum of *Arl13b*$^{R79Q/R79Q}$ mice
417 is not significantly different in width compared to controls.
418 Overall, our data indicate ARL13B function is critical for both SCP targeting and
419 controlling cerebellar vermis width. At one level, our data implicate Hh signaling in the
420 etiology of the MTS since we show that SCP targeting requires SMO. However, at
421 another level, our data indicate that Hh-independent pathways are at play as we don't
422 observe Hh-dependent neural tube patterning defects in the presence of the JSRD-
423 causing *Arl13b*^{R79Q} allele. In other mouse models of JSRD where the hypoplasia is
424 specific to the cerebellar vermis, Wnt signaling is affected (Lancaster *et al.* 2011). Thus,
425 the MTS could be due to disruption of different pathways in the SCPs and the vermis.
426 This would imply that the 35 JSRD implicated genes all affect the distinct pathways in a
427 similar manner (Parisi 2019). Alternatively, the MTS may form due to alterations in any
428 of a few pathways – and it is even possible that alterations in one pathway could impact
429 other pathways – or the ability of cells to respond to those other pathways. Such a
430 model is hinted at by previous work showing interplay between the Hh and Wnt
431 pathways underlying the severity of hindbrain phenotypes (Hagemann and Scholpp
432 2012; Bashford and Subramanian 2019). While we haven't detected any changes in
433 Wnt response in the absence of ARL13B function, we may have not examined the

434 relevant biological process or used a sensitive enough readout (Horner and Caspary
435 2011). Parallel reasoning would thus suggest that while *Arl13b*$^{R79Q/R79Q}$ mice clearly
436 transduce Hh reasonably well, there may be subtle changes in Shh signaling or
437 changes that influence Wnt signaling. Our data are consistent with the complexity
438 exhibited by other JSRD mouse models examined to date (Delous *et al.* 2007; Garcia-
439 Gonzalo *et al.* 2011; Roberson *et al.* 2015; Bashford and Subramanian 2019).
440 In patients, the SCP targeting deficit appears more severe than what we
441 observed in the mice. Available methods for live-imaging and examination of post-
442 mortem tissues suggest a range of SCP decussation defects, with some tracts
443 appearing thickened on the ipsilateral side relative to their DCN (Yachnis and Rorke
444 1999; Poretti *et al.* 2007). Surprisingly, in the mutant mice we infer midline crossing of
445 the SCPs. In the case of the *Smo*$^{Nex\text{-}Cre}$ conditional mice, it is formally possible that the
446 SCPs do not rely on SMO for midline crossing but only for subsequent targeting to the
447 dorsal thalamus. The fact that the *Arl13b*$^{Nex\text{-}Cre}$ conditional mice display a highly similar
448 phenotype to the *Smo*$^{Nex\text{-}Cre}$ conditional mice makes this less likely, since ARL13B is
449 directly implicated in JSRD and regulates SMO-dependent axon guidance in other
450 contexts (Cantagrel *et al.* 2008; Ferent *et al.* 2019). It is also plausible that the protein
451 turnover driven by *Nex-Cre* completed after midline crossing occurred. *Nex-Cre*
452 expression initiates at E11.5 in the cells on the rhombic lip of the cerebellar anlage as
453 they start to migrate and be specified before occupying the deep cerebellar nuclei (Fink
454 *et al.* 2006; Goebbels *et al.* 2006). We expect deletion would occur in the precursors
455 and therefore the neurons of the DCN would not express protein. Finally, it is possible
456 that the mouse is not a valid system in which to model the SCP midline crossing defect.

457 This might explain why we saw no defects in the SCP targeting of the *Arl13b*$^{R79Q/R79Q}$
458 mice, as this is a constitutive mutation that requires no protein turnover, yet
459 homozygous expression of ARL13B^{R79Q} in patients results in the molar tooth sign, which
460 has been associated with failed decussation of white matter tracts (Quisling *et al.* 1999).
461 Indeed, other mouse mutants such as *Cep290* and *Ahi1* which recapitulate the
462 cerebellar vermis hypoplasia, also do not display midline crossing defects in the SCPs
463 (Lancaster *et al.* 2011). Whether this is due to anatomical distinctions between the
464 cerebellum in mouse and human or the genetic background on which these models
465 were examined are open questions. Recent work highlights clear molecular and
466 temporal differences between mouse and human cerebellar development (Haldipur *et*
467 *al.* 2019; Behesti *et al.* 2021).
468 Examining SCP projections is labor intensive and it has not been done
469 systematically among the JSRD mouse models (Bashford and Subramanian 2019; Guo
470 *et al.* 2019). While previous work showed that *Arl13b*$^{Nex\text{-}Cre}$ and *Inpp5e*$^{Nex\text{-}Cre}$ mice
471 exhibit SCP targeting deficits, here we pinpoint the *Arl13b*$^{Nex\text{-}Cre}$ defect as specific to the
472 projection to the dorsal thalamus (Guo *et al.* 2019). The projection to the ventral
473 thalamus remains intact, suggesting there is not a generalized deficit in axon outgrowth
474 within the tract. The work on the *Arl13b*$^{Nex\text{-}Cre}$ and *Inpp5e*$^{Nex\text{-}Cre}$ SCP targeting deficits
475 argue that PI3K/Akt signaling from within cilia led to the tract defects (Guo *et al.* 2019).
476 However, we found that cilia-excluded ARL13B mediated SCP targeting normally.
477 These conflicting results could be explained by differences in the experimental details
478 as the data supporting ciliary ARL13B function used a human ARL13B viral expression
479 construct to rescue conditionally-deleted mice whereas we used genetic mutations

480 engineered at the endogenous locus in this study. Alternatively, these data could
481 indicate that ARL13B plays an important cellular role in the ciliary trafficking of key
482 components needed for the PI3K/Akt pathways.

483 JSRD-causing mutations in ARL13B are generally restricted to the GTPase
484 domain of the protein, although two residues outside that domain are implicated in
485 disease (Cantagrel *et al.* 2008; Bachmann-Gagescu *et al.* 2015; Thomas *et al.* 2015;
486 Shaheen *et al.* 2016; Rafiullah *et al.* 2017). Based on other ARL proteins, ARL13B likely
487 assumes distinct conformations upon the binding either GDP or GTP, permitting
488 different binding partners or altering affinities for binding partners (Pasqualato *et al.*
489 2002; Miertzschke *et al.* 2014). None of the tested JSRD-causing mutations (R79Q,
490 Y86C or R200C) disrupt GTP binding or hydrolysis, however, all three mutations disrupt
491 ARL13B function as an ARL3 GEF (Ivanova *et al.* 2017). The arginine at this position is
492 located within the Switch 2 region of ARL13B and is conserved in humans, mice,
493 zebrafish and *Chlamydomonas* (Figure 3B). We were surprised that we were unable to
494 detect any defects in our mouse, as we expected to model some aspect of Joubert
495 syndrome. Humans with homozygous R79Q mutation exhibit motor and ocular defects
496 (among other symptoms), whereas *arl13b*-null zebrafish injected with human ARL13B-
497 R79Q mRNA only partially rescue the ciliopathy phenotypes of curved body axis and
498 cystic kidney (Cantagrel *et al.* 2008). These species-dependent differences emphasize
499 the importance of analyzing mutations expressed from the endogenous promoter over
500 the course of normal development. A recent study linked *arl13b* disruption during
501 zebrafish development to reduced granule and Purkinje cells through a down-regulation
502 of Wnt signaling (Zhu *et al.* 2020). Given that complete deletion of ARL13B impacts

503 broader biological processes in the cerebellum than the R79Q mutation and that the null
504 mutant misregulates Hh signaling whereas R79Q does not, we conclude that a subset
505 of ARL13B function is disrupted in JSRD.
506

507 ***Acknowledgements***
508 We are grateful to L. Mariani for her initial work on this project, R.E. Van Sciver and E.
509 Gigante for critical comments on the manuscript and J.G. Mulle for the statistical
510 consults.
511

512 ***Funding***
513 This work was supported by funding from National Institutes of Health grants
514 R01NS090029, R01GM110663 and R35GM122549 to T.C. and T32GM008490 and
515 F31NS101806 to S.K.S. with additional support from the Emory University Integrated
516 Cellular Imaging Microscopy Core of the Emory Neuroscience NINDS Core Facilities
517 grant, P30NS055077. This study was supported in part by the Mouse Transgenic and
518 Gene Targeting Core (TMF), which is subsidized by the Emory university School of
519 Medicine and is one of the Emory Integrated Core Facilities. Additional support was
520 provided by the National Center for Advancing Translational Sciences of the National
521 Institutes of Health under Award Number UL1TR000454. The content is solely the
522 responsibility of the authors and does not necessarily reflect the official views of the
523 National Institutes of Health
524

525 ***Conflicts of Interest***

526 The authors have no competing interests to declare.

527

528 ***Author contributions statement***

529 Author Contributions: Conceptualization T.C.; Methodology S.K.S. and A.B.L.;
530 Validation S.K.S. and A.B.L; Formal Analysis S.K.S. and A.B.L.; Investigation S.K.S.
531 and A.B.L.; Writing – Original Draft S.K.S. and T.C.; Writing – Review & Editing S.K.S.,
532 A.B.L. and T.C.; Visualization S.K.S. and A.B.L.; Supervision T.C.; Project
533 Administration T.C.; Funding Acquisition T.C.

534

535 ***References***

536 Abdelhamed, Z. A., D. I. Abdelmottaleb, M. E. El-Asrag, S. Natarajan, G. Wheway et al.,
537 2019 The ciliary Frizzled-like receptor Tmem67 regulates canonical Wwnt/beta-
538 catenin signalling in the developing cerebellum via Hoxb5. *Sci Rep.* **9:** 5446.
539 doi:10.1038/s41598-019-41940-5

540 Abdelhamed, Z. A., G. Wheway, K. Szymanska, S. Natarajan, C. Toomes et al., 2013
541 Variable expressivity of ciliopathy neurological phenotypes that encompass
542 Meckel-Gruber syndrome and Joubert syndrome is caused by complex de-
543 regulated ciliogenesis, Shh and Wnt signalling defects. *Hum Mol Genet.* **22:**
544 1358-1372. doi:10.1093/hmg/dds546

545 Aguilar, A., A. Meunier, L. Strehl, J. Martinovic, M. Bonniere et al., 2012 Analysis of
546 human samples reveals impaired SHH-dependent cerebellar development in
547 Joubert syndrome/Meckel syndrome. *Proc Natl Acad Sci U S A.* **109:** 16951-
548 16956. doi:10.1073/pnas.1201408109

549 Alkanderi, S., E. Molinari, R. Shaheen, Y. Elmaghloob, L. A. Stephen et al., 2018 ARL3
550 mutations cause Joubert syndrome by disrupting ciliary protein composition. *Am*
551 *J Hum Genet.* **103:** 612-620. doi:10.1016/j.ajhg.2018.08.015
552 Arts, H. H., D. Doherty, S. E. C van Beersum, M. A. Parisi, S. J. F. Letteboer et al., 2007
553 Mutations in the gene encoding the basal body protein RPGRIP1L, a
554 nephrocystin-4 interactor, cause Joubert syndrome. *Nat Genet.* **39:** 882-888.
555 doi:10.1038/ng2069
556 Asadollahi, R., J. E. Strauss, M. Zenker, O. Beuing, S. Edvardson et al., 2018 Clinical
557 and experimental evidence suggest a link between KIF7 and C5orf42-related
558 ciliopathies through Sonic Hedgehog signaling. *Eur J Hum Genet.* **26:** 197-209.
559 doi:10.1038/s41431-017-0019-9
560 Bachmann-Gagescu, R., J. C. Dempsey, I. G. Phelps, B. J. O'Roak, D. M. Knutzen et
561 al., 2015 Joubert syndrome: A model for untangling recessive disorders with
562 extreme genetic heterogeneity. *J Med Genet.* **52:** 514-522.
563 doi:10.1136/jmedgenet-2015-103087
564 Bachmann-Gagescu, R., J. C. Dempsey, S. Bulgheroni, M. L. Chen, S. D'Arrigo et al.,
565 2020 Healthcare recommendations for Joubert syndrome. *Am J Med Genet A*.
566 **182:** 229-249. doi:10.1002/ajmg.a.61399
567 Bashford, A. L., and V. Subramanian, 2019 Mice with a conditional deletion of Talpid3
568 (KIAA0586) - a model for Joubert syndrome. *J Pathol.* **248:** 396-408.
569 doi:10.1002/path.5271
570 Bay, S.N., A. B. Long, and T. Caspary, 2018 Disruption of the ciliary GTPpase Arl13b
571 suppresses Sonic hedgehog overactivation and inhibits medulloblastoma

572 formation. *Proc Natl Acad Sci U S A.* **115:** 1570-1575.
573 doi:10.1073/pnas.1706977115
574 Behesti, H. A. Kocabas, D. E. Buchholz, T. S. Carroll, and M. E. Hatten, 2021 Altered
575 temporal sequence of transcriptional regulators in the generation of human
576 cerebellar granule cells. bioRxiv. doi:10.1101/2021.01.17.427030 (Preprint
577 posted January 17, 2021).
578 Bielas, S. L., J. L. Silhavy, F. Brancati, M. V. Kisseleva, L. Al-Gazali et al., 2009
579 Mutations in INPP5E, encoding inositol polyphosphate-5-phosphatase E, link
580 phosphatidyl inositol signaling to the ciliopathies. *Nat Genet.* **41:** 1032-1036.
581 doi:10.1038/ng.423
582 Bimonte, S., A. De Angelis, L. Quagliata, F. Giusti, R. Tammaro et al., 2011 Ofd1 is
583 required in limb bud patterning and endochondral bone development. *Dev Biol.*
584 **349:** 179-191. doi:10.1016/j.ydbio.2010.09.020
585 Bohne, P., M. K. Schwarz, S. Herlitze, and M. D. Mark, 2019 A new projection from the
586 deep cerebellar nuclei to the hippocampus via the ventrolateral and laterodorsal
587 thalamus in mice. *Front Neural Circuits.* **13:** 51. doi:10.3389/fncir.2019.00051
588 Brancati, F., B. Dallapiccola, and E. M. Valente, 2010 Joubert syndrome and related
589 disorders. *Orphanet J Rare Dis.* **5:** 20. doi:10.1186/1750-1172-5-20
590 Breslow, D. K., S. Hoogendoorn, A. R. Kopp, D. W. Morgens, B. K. Vu et al., 2018 A
591 CRISPR-based screen for Hedgehog signaling provides insights into ciliary
592 function and ciliopathies. *Nat Genet.* **50:** 460-471. doi:10.1038/s41588-018-0054-
593 7

594 Briscoe, J., and J. Ericson J, 1999 The specification of neuronal identity by graded
595 Sonic Hedgehog signalling. *Semin Cell Dev Biol.* **10:** 353-362.
596 doi:10.1006/scdb.1999.0295
597 Cantagrel, V., J. L. Silhavy, S. L. Bielas, D. Swistun, S. E. Marsh et al., 2008 Mutations
598 in the cilia gene ARL13B lead to the classical form of Jjoubert syndrome. *Am J*
599 *Hum Genet.* **83:** 170-179. doi:10.1016/j.ajhg.2008.06.023
600 Casoni, F., L. Croci, F. Vincenti, P. Podini, M. Riba et al., 2020 ZFP423 regulates early
601 patterning and multiciliogenesis in the hindbrain choroid plexus. *Development.*
602 **147:** dev190173. doi:10.1242/dev.190173
603 Caspary, T., M. J. Garcia-Garcia, D. Huangfu, J. T. Eggenschwiler, M. R. Wyler et al.,
604 2002 Mouse Dispatched homolog1 is required for long-range, but not juxtacrine,
605 Hh signaling. *Curr Biol.* **12:** 1628-1632. doi:10.1016/s)960-9822(02)01147-8
606 Caspary, T., C. E. Larkins, and K. V. Anderson, 2007 The graded response to Sonic
607 Hedgehog depends on cilia architecture. *Dev Cell.* **12:** 767-778.
608 doi:10.1016/j.devcel.2007.03.004
609 Charron, F., E. Stein, J. Jeong, A. P. McMahon, and M. Tessier-Lavigne, 2003 The
610 morphogen sonic hedgehog is an axonal chemoattractant that collaborates with
611 netrin-1 in midline axon guidance. *Cell.* **113:** 11-23. doi:10.1016/s0092-
612 8674(03)00199-5
613 Chavez, M., S. Ena, J. Van Sande, A. de Kerchove d'Exaerde, S. Schurmans et al.,
614 2015 Modulation of ciliary phosphoinositide content regulates trafficking and
615 Sonic hedgehog signaling output. *Dev Cell.* **34:** 338-350.
616 doi:10.1016/j.devcel.2015.06.016

617 Chiang, C., Y. Litingtung, E. Lee, K. E. Young, J. L. Corden et al., 1996 Cyclopia and
618 defective axial patterning in mice lacking Ssonic hedgehog gene function.
619 *Nature.* **383:** 407-413. Doi:10.1038/383407a0
620 Chih, B., P. Liu, Y. Chinn, C. Chalouni, L. G. Komuves et al., 2011 A ciliopathy complex
621 at the transition zone protects the cilia as a privileged membrane domain. *Nat*
622 *Cell Biol.* **14:** 61-72. doi:10.1038/ncb2410
623 Chizhikov, V. V., J. Davenport, Q. Zhang, E. K. Shih, O. A. Cabello et al., 2007 Cilia
624 proteins control cerebellar morphogenesis by promoting expansion of the granule
625 progenitor pool. *J Neurosci.* **27:** 9780-9789. doi:10.1523/JNEUROSCI.5586-
626 06.2007
627 Christopher, K. J., B. Wang, Y. Kong, and S. D. Weatherbee, 2012 Forward genetics
628 uncovers Transmembrane protein 107 as a novel factor required for ciliogenesis
629 and Sonic hedgehog signaling. *Dev Biol.* **368:** 382-392.
630 doi:10.1016/j.ydbio.2012.06.008
631 Constable, S., A. B. Long, K. A. Floyd, S. Schurmans, and T. Caspary, 2020 The ciliary
632 phosphatidylinositol phosphatase Inpp5e plays positive and negative regulatory
633 roles in Shh signaling. *Development.* **147:** dev183301. doi:10.1242/dev.183301
634 Consugar, M. B., V. J. Kubly, D. J. Lager, C. J. Hommerding, W. C. Wong et al., 2007
635 Molecular diagnostics of Meckel–Gruber syndrome highlights phenotypic
636 differences between MKS1 and MKS3. *Hum Genet.* **121:** 591-599.
637 doi:10.1007/s00439-007-0341-3
638 Dahmane, N., and A. Ruiz i Altaba, 1999 Sonic hedgehog regulates the growth and
639 patterning of the cerebellum. *Development.* **126:** 3089-3100.

640 Davey, M. G., I. R. Paton, Y. Yin, M. Schmidt, F. K. Bangs et al., 2006 The chicken
641 talpid3 gene encodes a novel protein essential for Hedgehog signaling. *Genes*
642 *Dev.* **20:** 1365-1377. doi:10.1101/gad.369106
643 Delous, M., L. Baala, R. Salomon, C. Laclef, J. Vierkotten et al., 2007 The ciliary gene
644 RPGRIP1L is mutated in cerebello-oculo-renal syndrome (Joubert syndrome type
645 B) and Meckel syndrome. *Nat Genet.* **39:** 875-881. doi:10.1038/ng2039
646 Deshpande, O., R. Z. Lara, O. R. Zhang, D. Concepcion, and B. A. Hamilton, 2020
647 ZNF423 patient variants, truncations, and in-frame deletions in mice define an
648 allele-dependent range of midline brain abnormalities. *PLoS Genet.* **16:**
649 e1009017. doi:10.1371/journal.pgen.1009017
650 Doherty, D., 2009 Joubert syndrome: Insights into brain development, cilium biology,
651 and complex disease. *Semin Pediatr Neurol.* **16:** 143-154.
652 doi:10.1016/j.spen.2009.06.002
653 Dowdle, W. E., J. F. Robinson, A. Kneist, M. S. Sirerol-Piquer, S. G. M. Frints et al.,
654 2011 Disruption of a ciliary B9 protein complex causes Meckel syndrome. *Am J*
655 *Hum Genet.* **89:** 94-110. doi:10.1016/j.ajhg.2011.06.003
656 Ferent, J., S. Constable, E. D. Gigante, P. T. Yam, L. E. Mariani et al., 2019 The ciliary
657 protein Arl13b functions outside of the primary cilium in Shh-mediated axon
658 guidance. *Cell Rep.* **29:** 3356-3366.e3353. doi:10.1016/j.celrep.2019.11.015
659 Fink, A. J., C. Englund, R. A. M. Daza, D. Pham, C. Lau et al., 2006 Development of
660 the deep cerebellar nuclei: Transcription factors and cell migration from the
661 rhombic lip. *J Neurosci.* **26:** 3066-3076. doi:10.1523/JNEUROSCI.5203-05.2006

662 Frikstad, K-A. M., E. Molinari, M. Thoresen, S. A. Ramsbottom, F. Hughes et al., 2019
663 A CEP104-CSPP1 complex is required for formation of primary cilia competent in
664 Hedgehog signaling. *Cell Rep.* **28:** 1907-1922.e6
665 doi:10.1016/j.celrep.2019.07.025
666 Garcia-Gonzalo, F. R., K. C. Corbit, M. S. Sirerol-Piquer, G. Ramaswami, E. A. Otto et
667 al., 2011 A transition zone complex regulates mammalian ciliogenesis and ciliary
668 membrane composition. *Nat Genet.* **43:** 776-784. doi:10.1038/ng.891
669 Garcia-Gonzalo, F. R., S. C. Phua, E. C. Roberson, G. Garcia 3rd, M. Abedin et al.,
670 2015 Phosphoinositides regulate ciliary protein trafficking to modulate Hedgehog
671 signaling. *Dev Cell.* **34:** 400-409. doi:10.1016/j.devcel.2015.08.001
672 Gaudet, M., A-G. Fara, I. Beritognolo, and M. Sabatti, 2009 Allele-specific PCR in SNP
673 genotyping. *Methods Mol Biol.* **578:** 415-424. doi:10.1007/978-1-60327-411-1_26
674 Gigante, E. D., M. R. Taylor, A. A. Ivanova, R. A. Kahn, and T. Caspary, 2020. ARL13B
675 regulates Sonic hedgehog signaling from outside primary cilia. *eLife.* **9:** e50434.
676 doi:10.7554/eLife.50434
677 Goebbels, S., I. Bormuth, U. Bode, O. Hermanson, M. H. Schwab et al., 2006 Genetic
678 targeting of principal neurons in neocortex and hippocampus of NEX-Cre mice.
679 *Genesis.* **44:** 611-621. doi:10.1002/dvg.20256
680 Gotthardt, K., M. Lokaj, C. Koerner, N. Falk, A. Giessl et al., 2015 A G-protein
681 activation cascade from Arl13b to Arl3 and implications for ciliary targeting of
682 lipidated proteins. *eLife.* **4:** e11859. doi:10.7554/eLife.11859

683 Guo, J., J. M. Otis, S. K. Suciu, C. Catalano, L. Xing et al., 2019 Primary cilia signaling
684 promotes axonal tract development and is disrupted in Joubert syndrome-related
685 disorders models. *Dev Cell.* **51:** 759-774 e755. doi:10.1016/j.devcel.2019.11.005
686 Hagemann, A. I. H., and S. Scholpp, 2012 The tale of the three brothers – Shh, Wnt,
687 and Fgf during development of the thalamus. *Front Neurosci.* **6:** 76.
688 doi:10.3389/fnins.2012.00076
689 Haldipur, P., K. A. Aldinger, S. Bernardo, M. Deng, A. E. Timms et al., 2019
690 Spatiotemporal expansion of primary progenitor zones in the developing human
691 cerebellum. *Science*. **366:** 454-460. Doi: 10.1126/science.aax7526
692 Hata, A., J. Seoane, G. Lagna, E. Montalvo, A. Hemmati-Brivanlou et al., 2000 OAZ
693 uses distinct DNA- and protein-binding zinc fingers in separate BMP-Smad and
694 Olf signaling pathways. *Cell.* **100:** 229-240. doi:10.1016/s0092-8674(00)81561-5
695 Hazen, V. M. , M. G. Andrews, L. Umans, E. B. Crenshaw 3rd, A. Zwijsen et al., 2012
696 BMP receptor-activated Smads confer diverse functions during the development
697 of the dorsal spinal cord. *Dev Biol.* **367:** 216-227.
698 doi:10.1016/j.ydbio.2012.05.014
699 Heydemann, A., L. C. Nguyen, and E. B. Crenshaw 3rd, 2001 Regulatory regions from
700 the Brn4 promoter direct LACZ expression to the developing forebrain and neural
701 tube. *Brain Res Dev Brain Res.* **128:** 83-90. doi:10.1016/s0165-3806(01)00137-7
702 Hopp, K., C. M. Heyer, C. J. Hommerding, S. A. Henke, J. L. Sundsbak et al., 2011
703 B9D1 is revealed as a novel Meckel syndrome (MKS) gene by targeted exon-
704 enriched next-generation sequencing and deletion analysis. *Hum Mol Genet.* **20:**
705 2524-2534. doi:10.1093/hmg/ddr151

706 Horner, V. L., and T. Caspary, 2011 Disrupted dorsal neural tube BMP signaling in the
707 cilia mutant Arl13b hnn stems from abnormal Shh signaling. *Dev Biol.* **355:** 43-
708 54. doi:10.1016/j.ydbio.2011.04.019
709 Huang, S., J. Laoukili, M. T. Epping, J. Koster, M. Hölzel et al., 2009 ZNF423 is
710 critically required for retinoic acid-induced differentiation and is a marker of
711 neuroblastoma outcome. *Cancer Cell.* **15:** 328-340.
712 doi:10.1016/j.ccr.2009.02.023
713 Huangfu, D., A. Liu, A. S. Rakeman, N. S. Murcia, L. Niswander et al., 2003 Hedgehog
714 signalling in the mouse requires intraflagellar transport proteins. *Nature.* **426:** 83-
715 87. doi:10.1038/nature02061
716 Humbert, M. C., K. Weihbrecht, C. C. Searby, Y. Li, R. M. Pope et al., 2012 ARL13B,
717 PDE6D, and CEP164 form a functional network for INPP5E ciliary targeting. *Proc*
718 *Natl Acad Sci U S A.* **109:** 19691-19696. doi:10.1073/pnas.1210916109
719 Hynes, A. M., R. H. Giles, S. Srivastava, L. Eley, J. Whitehead et al., 2014 Murine
720 Joubert syndrome reveals Hedgehog signaling defects as a potential therapeutic
721 target for nephronophthisis. *Proc Natl Acad Sci U S A.* **111:** 9893-9898.
722 doi:10.1073/pnas.1322373111
723 Ivanova, A. A., T. Caspary, N. T. Seyfried, D. M. Duong, A. B. West et al., 2017
724 Biochemical characterization of purified mammalian ARL13B protein indicates
725 that it is an atypical GTPase and ARL3 guanine nucleotide exchange factor
726 (GEF). *J Biol Chem.* **292:** 11091-11108. doi:10.1074/jbc.M117.784025
727 Kenney, A. M., and D. H. Rowitch, 2000 Sonic hedgehog promotes G(1) cyclin
728 expression and sustained cell cycle progression in mammalian neuronal

729 precursors. *Mol Cell Biol.* **20:** 9055-9067. doi:10.1128/mcb.20.23.9055-
730 9067.2000
731 Lai, C. K., N. Gupta, X. Wen, L. Rangell, B. Chih et al., 2011 Functional
732 characterization of putative cilia genes by high-content analysis. *Mol Biol Cell.*
733 **22:** 1104-1119. doi:10.1091/mbc.E10-07-0596
734 Lan, Y., and R. Jiang, 2009 Sonic hedgehog signaling regulates reciprocal epithelial-
735 mesenchymal interactions controlling palatal outgrowth. *Development*. **136:**
736 1387-1396. doi:10.1242/dev.028167
737 Lancaster, M. A., D. J. Gopal, J. Kim, S. N. Saleem, J. L. Silhavy et al., 2011 Defective
738 Wnt-dependent cerebellar midline fusion in a mouse model of Joubert syndrome.
739 *Nat Med.* **17:** 726-731. doi:10.1038/nm.2380
740 Li, Y., Q. Wei, Y. Zhang, K. Ling, and J. Hu, 2010 The small GTPases ARL-13 and
741 ARL-3 coordinate intraflagellar transport and ciliogenesis. *J Cell Biol.* **189:** 1039-
742 1051. doi:10.1083/jcb.200912001
743 Li, Y., X. Tian, M. Ma, S. Jerman, S. Kong et al., 2016 Deletion of ADP ribosylation
744 factor-like GTPase 13B leads to kidney cysts. *J Am Soc Nephrol.* **27:** 3628-3638.
745 doi:10.1681/ASN.2015091004
746 Lipinski, R. J., C. Song, K. K. Sulik, J. L. Everson, J. J. Gipp et al., 2010 Cleft lip and
747 palate results from Hedgehog signaling antagonism in the mouse: Phenotypic
748 characterization and clinical implications. *Birth Defects Res A Clin Mol Teratol.*
749 **88:** 232-240. doi:10.1002/bdra.20656

750 Maria, B. L., K. B. Hoang, R. J. Tusa, A. A. Mancuso, L. M. Hamed et al., 1997 "Joubert
751 syndrome" revisited: key ocular motor signs with magnetic resonance imaging
752 correlation. *J Child Neurol.* **12:** 423-430. doi:10.1177/088307389701200703
753 Mariani, L. E., M. F. Bijlsma, A. A. Ivanova, S. K. Suciu, R. A. Kahn et al., 2016 Arl13b
754 regulates Shh signaling from both inside and outside the cilium. *Mol Biol Cell.* **27:**
755 3780-3790. doi:10.1091/mbc.E16-03-0189
756 Miertzschke, M., C. Koerner, M. Spoerner, and A. Wittinghofer, 2014 Structural insights
757 into the small G-protein Arl13b and implications for Joubert syndrome. *Biochem*
758 *J.* **457:** 301-311. doi:10.1042/BJ20131097
759 Munoz-Estrada, J., and R. J. Ferland, 2019 Ahi1 promotes Arl13b ciliary recruitment,
760 regulates Arl13b stability and is required for normal cell migration. *J Cell Sci.*
761 **132:** jcs230680. doi:10.1242/jcs.230680
762 Nolan-Stevaux, O., J. Lau, M. L. Truitt, G. C. Chu, M. Hebrok et al., 2009 Gli1 is
763 regulated through Smoothened-independent mechanisms in neoplastic
764 pancreatic ducts and mediates PDAC cell survival and transformation. *Genes*
765 *Dev.* **23:** 24-36. doi:10.1101/gad.1753809
766 Nuovo, S., I. Bacigalupo, M. Ginevrino, R. Battini, E. Bertini et al., 2020 Age and sex
767 prevalence estimate of Joubert syndrome in Italy. *Neurology*. **94:** e797-e801.
768 doi:10/1212/WNL.0000000000008996
769 Onimaru, H., Y. Kumagawa, and I. Homma, 2006 Respiration-related rhythmic activity
770 in the rostral medulla of newborn rats. *J Neurophysiol.* **96:** 55-61.
771 doi:10.1152/jn.01175.2005

772 Otto, E. A., K. Tory, M. Attanasio, W. Zhou, M. Chaki et al, 2009 Hypomorphic
773 mutations in meckelin (MKS3/TMEM67) cause nephronophthisis with liver
774 fibrosis (NPHP11). *J Med Genet.* **46:** 663-670. doi:10.1136/jmg.2009.066613
775 Parisi, M. A, 2019 The molecular genetics of Joubert syndrome and related ciliopathies:
776 The challenges of genetic and phenotypic heterogeneity. *Transl Sci Rare Dis.* **4:**
777 25-49. doi:10.3233/TRD-190041
778 Parisi, M. A., D. Doherty, P. F. Chance, and I. A. Glass, 2007 Joubert syndrome (and
779 related disorders) (OMIM 213300). *Eur J Hum Genet.* **15:** 511-521.
780 doi:10.1038/sj.ejhg.5201648
781 Pasqualato, S., L. Renault, and J. Cherfils, 2002 Arf, Arl, Arp and Sar proteins: A family
782 of GTP-binding proteins with a structural device for 'front-back' communication.
783 *EMBO Rep.* **3:** 1035-1041. doi:10.1093/embo-reports/kvf221
784 Poretti, A., E. Boltshauser, T. Loenneker, E. M. Valente, F. Brancati et al., 2007
785 Diffusion tensor imaging in Joubert syndrome. *AJNR Am J Neuroradiol.* **28:**
786 1929-1933. doi:10.3174/ajnr.A0703
787 Quisling, R. G., A. J. Barkovich, and B. L. Maria, 1999 Magnetic resonance imaging
788 features and classification of central nervous system malformations in Joubert
789 syndrome. *J Child Neurol.* **14:** 628-635. doi:10.1177/088307389901401002
790 Rafiullah, R., A. B. Long, A. A. Ivanova, H. Ali, S. Berkel et al., 2017 A novel
791 homozygous ARL13B variant in patients with Joubert syndrome impairs its
792 guanine nucleotide-exchange factor activity. *Eur J Hum Genet.* **25:** 1324-1334.
793 doi:10.1038/s41431-017-0031-0

794 Ramsbottom, S. A., P. E. Thelwall, K. M. Wood, G. J. Clowry, L. A. Devlin et al., 2020
795 Mouse genetics reveals Barttin as a genetic modifier of Joubert syndrome. *Proc*
796 *Natl Acad Sci U S A.* **117:** 1113-1118. doi:10.1073/pnas.1912602117
797 Reiter, J. F., and W. C. Skarnes, 2006 Tectonic, a novel regulator of the Hedgehog
798 pathway required for both activation and inhibition. *Genes Dev.* **20:** 22-27.
799 doi:10.1101/gad.1363606
800 Roberson, E. C., W. E. Dowdle, A. Ozanturk, F. R. Garcia-Gonzalo, C. Li et al., 2015
801 TMEM231, mutated in orofaciodigital and Meckel syndromes, organizes the
802 ciliary transition zone. *J Cell Biol.* **209:** 129-142. doi:10.1083/jcb.201411087
803 Sang, L., J. J. Miller, K. C. Corbit, R. H. Giles, M. J. Brauer et al., 2011 Mapping the
804 NPHP-JBTS-MKS protein network reveals ciliopathy disease genes and
805 pathways. *Cell.* **145:** 513-528. doi:10.1016/j.cell.2011.04.019
806 Schindelin, J., I. Arganda-Carreras, E. Frise, V. Kaynig, M. Longair et al., 2012 Fiji: an
807 open-source platform for biological-image analysis. *Nat Methods.* **9:** 676-682.
808 doi:10.1038/nmeth.2019
809 Schrick, J. J., P. Vogel, A. Abuin, B. Hampton, and D. S. Rice, 2006 ADP-ribosylation
810 factor-like 3 is involved in kidney and photoreceptor development. *Am J Pathol.*
811 **168:** 1288-1298. doi:10.2353/ajpath.2006.050941
812 Schwarz, N., A. Lane, K. Jovanovic, D. A. Parfitt, M. Aguila et al., 2017 Arl3 and RP2
813 regulate the trafficking of ciliary tip kinesins. *Hum Mol Genet.* **26:** 2480-2492.
814 doi:10.1093/hmg/ddx143

815 Shaheen, R., K. Szymanska, B. Basu, N. Patel, N. Ewida et al., 2016 Characterizing
816 the morbid genome of ciliopathies. *Genome Biol.* **17:** 242. doi:10.1186/s13059-
817 016-1099-5
818 Srour, M., F. F. Hamdan, J. A. Schwartzentruber, L. Patry, L. H. Ospina et al., 2012
819 Mutations in TMEM231 cause Joubert syndrome in French Canadians. *J Med*
820 *Genet.* **49:** 636-641. doi:10.1136/jmedgenet-2012-101132
821 Su, C-Y., S. N. Bay, L. E. Mariani, M. J. Hillman, and T. Caspary, 2012 Temporal
822 deletion of Arl13b reveals that a mispatterned neural tube corrects cell fate over
823 time. *Development.* **139:** 4062-4071. doi:10.1242/dev.082321
824 Thomas, S., V. Cantagrel, L. Mariani, V. Serre, J-E. Lee et al., 2015 Identification of a
825 novel ARL13B variant in a Joubert syndrome-affected patient with retinal
826 impairment and obesity. *Eur J Hum Genet.* **23:** 621-627.
827 doi:10.1038/ejhg.2014.156
828 Thomas, S., M. Legendre, S. Saunier, B. Bessières, C. Alby et al., 2012 TCTN3
829 mutations cause Mohr-Majewski syndrome. *Am J Hum Genet.* **91:** 372-378.
830 doi:10.1016/j.ajhg.2012.06.017
831 Valente, E. M., F. Brancati, and B. Dallapiccola, 2008 Genotypes and phenotypes of
832 Joubert syndrome and related disorders. *Eur J Med Genet.* **51:** 1-23.
833 doi:10.1016/j.ejmg.2007.11.003
834 Valente, E. M., C. V. Logan, S. Mougou-Zerelli, J. H. Lee, J. L. Silhavy et al., 2010
835 Mutations in TMEM216 perturb ciliogenesis and cause Joubert, Meckel and
836 related syndromes. *Nat Genet.* **42:** 619-625. doi:10.1038/ng.594

837 Vierkotten, J., R. Dildrop, T. Peters, B. Wang, and U. Rüther, 2007 Ftm is a novel basal
838 body protein of cilia involved in Shh signaling. *Development.* **134:** 2569-2577.
839 doi:10.1242/dev.003715
840 Weatherbee, S. D., L. A. Niswander, and K. V. Anderson, 2009 A mouse model for
841 Meckel syndrome reveals Mks1 is required for ciliogenesis and Hedgehog
842 signaling. *Hum Mol Genet.* **18:** 4565-4575. doi:10.1093/hmg/ddp422
843 Wechsler-Reya, R. J., and M. P. Scott, 1999 Control of neuronal precursor proliferation
844 in the cerebellum by Sonic Hedgehog. *Neuron.* **22:** 103-114. doi:10.1016/s0896-
845 6273(00)80682-0
846 Wu, C., M. Yang, J. Li, C. Wang, T. Cao et al., 2014 Talpid3-binding centrosomal
847 protein Cep120 is required for centriole duplication and proliferation of cerebellar
848 granule neuron progenitors. *PLoS One.* **9:** e107943.
849 doi:10.1371/journal.pone.0107943
850 Yachnis, A. T., and L. B. Rorke, 1999 Neuropathology of Joubert syndrome. *J Child*
851 *Neurol.* **14:** 655-659. doi:10.1177/088307389901401006
852 Zhang, X. M., M. Ramalho-Santos, and A. P. McMahon, 2001 Smoothened mutants
853 reveal redundant roles for Shh and Ihh signaling including regulation of L/R
854 symmetry by the mouse node. *Cell.* **106:** 781-792.
855 Zhu, J., H.-T. Wang, Y.-R. Chen, L.-Y. Yan, Y.-Y. Han et al., 2020 The Joubert
856 syndrome gene arl13b is critical for early cerebellar development in zebrafish.
857 *Neurosci Bull.* **36:** 1023-1034. doi:10.1007/s12264-020-00554-y
858
859 ***Figure legends***

860 **Figure 1: SCPs lacking *Arl13b* or *Smo* fail to project to the dorsal thalamus.** (A-C)
861 Schematics of injections and fluorescent tracer diffusion shown horizontally (A) or
862 sagittally (B-C). (A) Red dashed arrow depicts dye path in a successful injection from
863 injection site (red X) caudal through the brain and across the midline and into the
864 contralateral cerebellar DCN (red arrowhead). Grey background boxes indicate area of
865 subsequent images: the injection site (INJ) and cerebellum (DCN). (D-I) Representative
866 images of dorsal (D, F, H) or ventral (E, G, I) thalamus injection site (top panel) and
867 cerebellum (middle panel) with the DCN in hatched white circle and magnified (bottom
868 panel) with recoloring to black and white to aid visualization. The retrograde fluorescent
869 tracer is pink-red and sections are stained with DAPI (blue). Numbers indicate the
870 number of positively stained DCN clusters (DCN traced) out of the total number of
871 injected animals. Note that no tracing was observed on ipsilateral side to injection. (D,
872 E) Fluorescent tracer injection in *Smo*$^{fl/+}$*; Arl13b*$^{fl/+}$*; Nex-Cre* control animals resulted in
873 contralateral DCN staining in (D) 6/8 dorsal thalamus injections and (E) 8/11 ventral
874 thalamus injections. (F, G) Fluorescent tracer injection in *Smo*$^{Nex\text{-}Cre}$ animals resulted in
875 contralateral DCN staining in (F) 0/6 dorsal thalamus injections and (G) 4/4 ventral
876 thalamus injections. (H, I) Fluorescent tracer injection in *Arl13b*$^{Nex\text{-}Cre}$ animals resulted in
877 contralateral DCN staining in (H) 1/7 dorsal thalamus injections and (I) 4/4 ventral
878 thalamus injections. Two-tailed Fisher's exact test was performed; only the dorsal
879 injection results were significantly different from the controls (F: $p<0.01$; H: $p<0.05$)
880
881 **Figure 2: SCPs expressing cilia-excluded ARL13B^{V358A} project normally to both**
882 **the dorsal and ventral thalamus.** (A-D) Representative images of dorsal (A, C) or

883 ventral (B, D) thalamus injection site (top panel) and cerebellum (middle panel) with the
884 DCN in hatched white circle and magnified (bottom panel) with recoloring to black and
885 white to aid visualization. Numbers indicate the number of positively stained DCN
886 clusters out of the total number of injected animals. Note that no tracing was observed
887 on the injection's ipsilateral side. (A, B) Fluorescent tracer injection in *Arl13b*$^{V358A/+}$
888 control animals resulted in contralateral DCN staining in (A) 3/3 dorsal thalamus
889 injections and (B) 4/4 ventral thalamus injections. (C-D) Fluorescent tracer injection in
890 *Arl13b*$^{V358A/V358A}$ animals resulted in contralateral DCN staining in (C) 4/4 dorsal
891 thalamus injections (Fisher's exact test, two-tailed, ns, p>0.9) and (D) 3/3 ventral
892 thalamus injections (ns, p>0.9).
893
894 **Figure 3: SCPs expressing JS allele *Arl13b*^{R79Q} project normally to both the dorsal**
895 **and ventral thalamus.** (A) Schematic showing the protein domain structure of Arl13b.
896 The R79Q mutation occurs in a highly conserved subregion of the GTPase domain,
897 Switch 2 (red). (B) Alignment of protein sequence surrounding amino acid 79 of mouse
898 Arl13b (red highlight) showing that arginine is conserved across multiple species.
899 Sequences used in protein alignment: *Homo sapiens* NP_878899.1, *Mus musculus*
900 NP_080853.3, *Danio rerio* NP_775379.1, *Chlamydomonas reinhardtii* XP_001691430.1.
901 (C-F) Representative images of dorsal (C, E) or ventral (D, F) thalamus injection site
902 (top panel) and cerebellum (middle panel) with the DCN in hatched white circle and
903 magnified (bottom panel) with recoloring to black and white to aid visualization.
904 Numbers indicate the number of positively stained DCN clusters out of the total number
905 of injected animals. Note that no tracing was observed on the injection's ipsilateral side.

906 (C, D) Fluorescent tracer injection in *Arl13b*$^{R79Q/+}$ control animals resulted in
907 contralateral DCN staining in (C) 4/4 dorsal thalamus injections and (D) 3/3 ventral
908 thalamus injections. (E-F) Fluorescent tracer injection in *Arl13b*$^{R79Q/R79Q}$ animals
909 resulted in contralateral DCN staining in (E) 3/3 dorsal thalamus injections (Fisher's
910 exact test, two-tailed, ns, p>0.9) and (F) 3/4 ventral thalamus injections (ns, p>0.9).
911
912 **Figure 4: Mouse embryos expressing JS allele *Arl13b*^{R79Q} display normal cell**
913 **patterning in the neural tube.** Shh, Olig2, Pax6 and Arl13b staining of E10.5 *Arl13b*$^{+/+}$
914 (n=3), *Arl13b*$^{R79Q/R79Q}$ (n=3), *Arl13b*$^{R79Q/\Delta}$ (n=3), and *Arl13b*$^{\Delta/\Delta}$ (n=3) mouse neural tubes.
915 Scale bar = 100 micrometers in A-L or 10 micrometers in M-P. (A-D) Shh is visible in the
916 notochord and floorplate of (A) *Arl13b*$^{+/+}$, (B) *Arl13b*$^{R79Q/R79Q}$ and (C) *Arl13b*$^{R79Q/\Delta}$ neural
917 tubes but absent from the floorplate of (D) *Arl13b*$^{\Delta/\Delta}$ embryos. (E-H) Olig2 stains the
918 motor neuron precursor domain in (E) *Arl13b*$^{+/+}$, (F) *Arl13b*$^{R79Q/R79Q}$ and (G) *Arl13b*$^{R79Q/\Delta}$
919 embryos and stains an expanded domain in (H) *Arl13b*$^{\Delta/\Delta}$ embryos. (I-L) Pax6
920 expression is visible in the dorsal neural tube in (I) *Arl13b*$^{+/+}$, (J) *Arl13b*$^{R79Q/R79Q}$ and (K)
921 *Arl13b*$^{R79Q/\Delta}$ neural tubes but shifted dorsally in (L) *Arl13b*$^{\Delta/\Delta}$ neural tubes. (M-P) Arl13b
922 is localized to cilia visible in the ventral lumen of (M) *Arl13b*$^{+/+}$, (N) *Arl13b*$^{R79Q/R79Q}$ and
923 (O) *Arl13b*$^{R79Q/\Delta}$ neural tubes but absent from (P) *Arl13b*$^{\Delta/\Delta}$ embryos.
924
925 **Figure 5: *Arl13b*^{R79Q} mutation does not affect cerebellar width.** (A) Representative
926 surface-facing images of cerebella from control and *Arl13b*$^{R79Q/R79Q}$ mutant mice.
927 Scalebar = 1mm, black line indicates where cerebellar width was measured, red line
928 indicates where vermis width was measured, gray line indicates where cerebellar

929 hemisphere height was measured, blue line indicates where vermis height was
930 measured. (B) Ratios of *Arl13b*$^{R79Q/R79Q}$ mutant to control measurements of sex- and
931 age-matched pairs of mice showed no significant difference. Cerebellar and vermis
932 measurements were determined from surface views (symbol colors match the lines in
933 A), body and dissected brain weights were determined using a standard lab scale. Each
934 symbol represents a pair of sex- and age-matched animals: females are represented as
935 circles and males are represented as triangles.
936
937 **Figure 6: Pan-neuronal deletion of *Arl13b* results in a small cerebellum.** (A)
938 Representative images of cerebella from control and *Arl13b*$^{Brn4\text{-}Cre}$ mutant mice.
939 Scalebar = 1mm. (B) The ratio of *Arl13b*$^{Brn4\text{-}Cre}$ mutant to control cerebellar width was
940 reduced in both females and males (one-sample t-test: $p<0.1$, single asterisk). The ratio
941 of *Arl13b*$^{Brn4\text{-}Cre}$ mutant to control vermis width was reduced in female and male age
942 matched pairs (one-sample t-test: $p<0.0001$, four asterisks). While *Arl13b*$^{Brn4\text{-}Cre}$ mutants
943 had moderately lower body weights than controls (one-sample t-test: $p<0.1$, single
944 asterisk), their brains were slightly heavier, likely due to hydrocephaly. Each symbol
945 represents a pair of sex- and age-matched animals: females are represented as circles
946 and males are represented as triangles.
947
948 **Figure 7: Mice expressing cilia-excluded *Arl13b*^{V358A} have cerebella of normal**
949 **width.** (A) Representative images of cerebella from control and *Arl13b*$^{V358A/V358A}$ mutant
950 mice. Scalebar = 1mm. (B) Ratios of *Arl13b*$^{V358A/V358A}$ mutant to control measurements
951 of sex- and age-matched pairs of mice showed no significant differences (one-sample t-

952 test). Each dot represents a pair of sex- and age-matched animals: females are

953 represented as circles and males are represented as triangles.

954

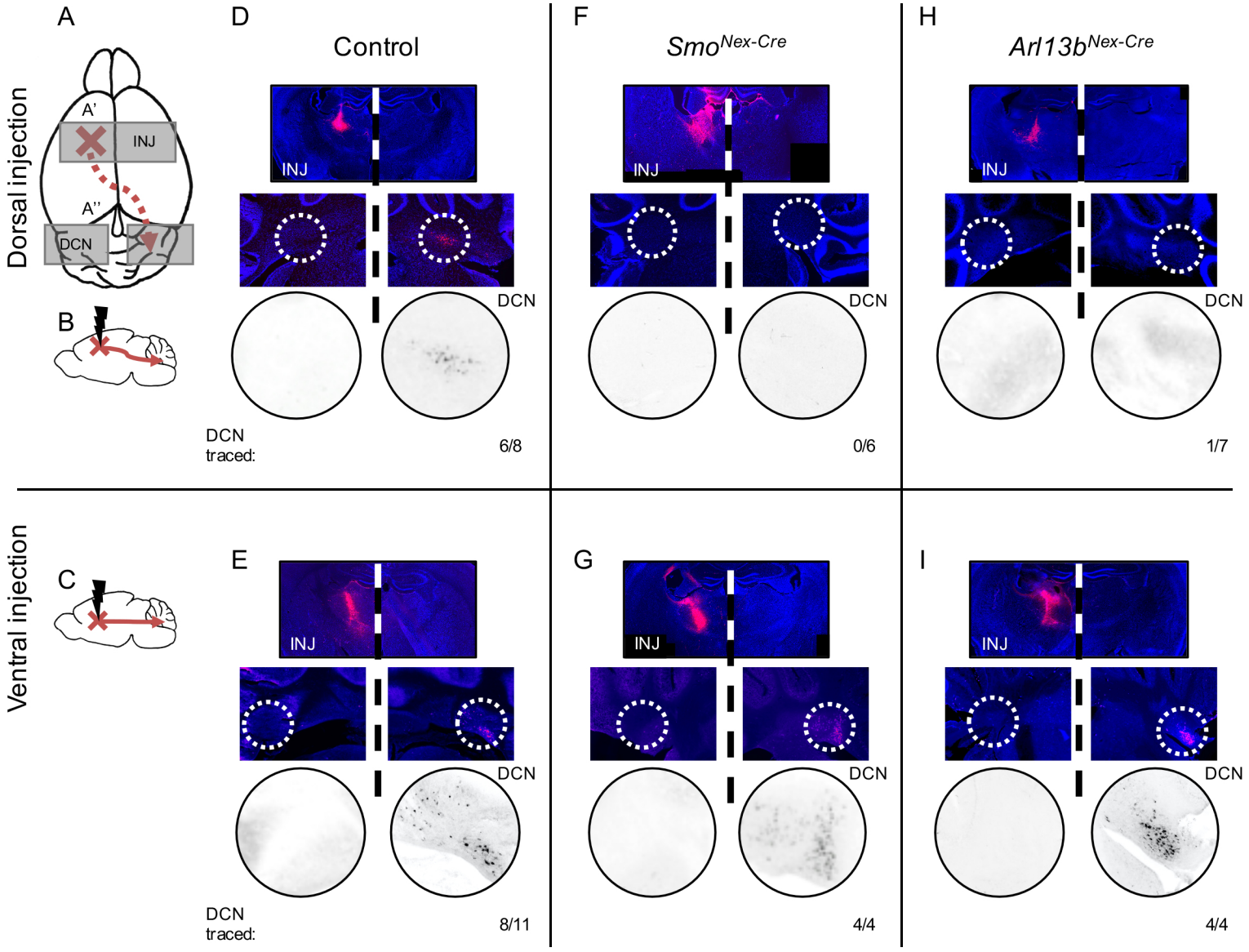
A
Dorsal injection
A'
INJ
A''
DCN
B
C
Ventral injection
D
Control
INJ
DCN
DCN traced:
6/8
E
INJ
DCN
DCN traced:
8/11
F
Smo^Nex-Cre
INJ
DCN
0/6
G
INJ
DCN
4/4
H
Arl13b^Nex-Cre
INJ
DCN
1/7
I
INJ
DCN
4/4

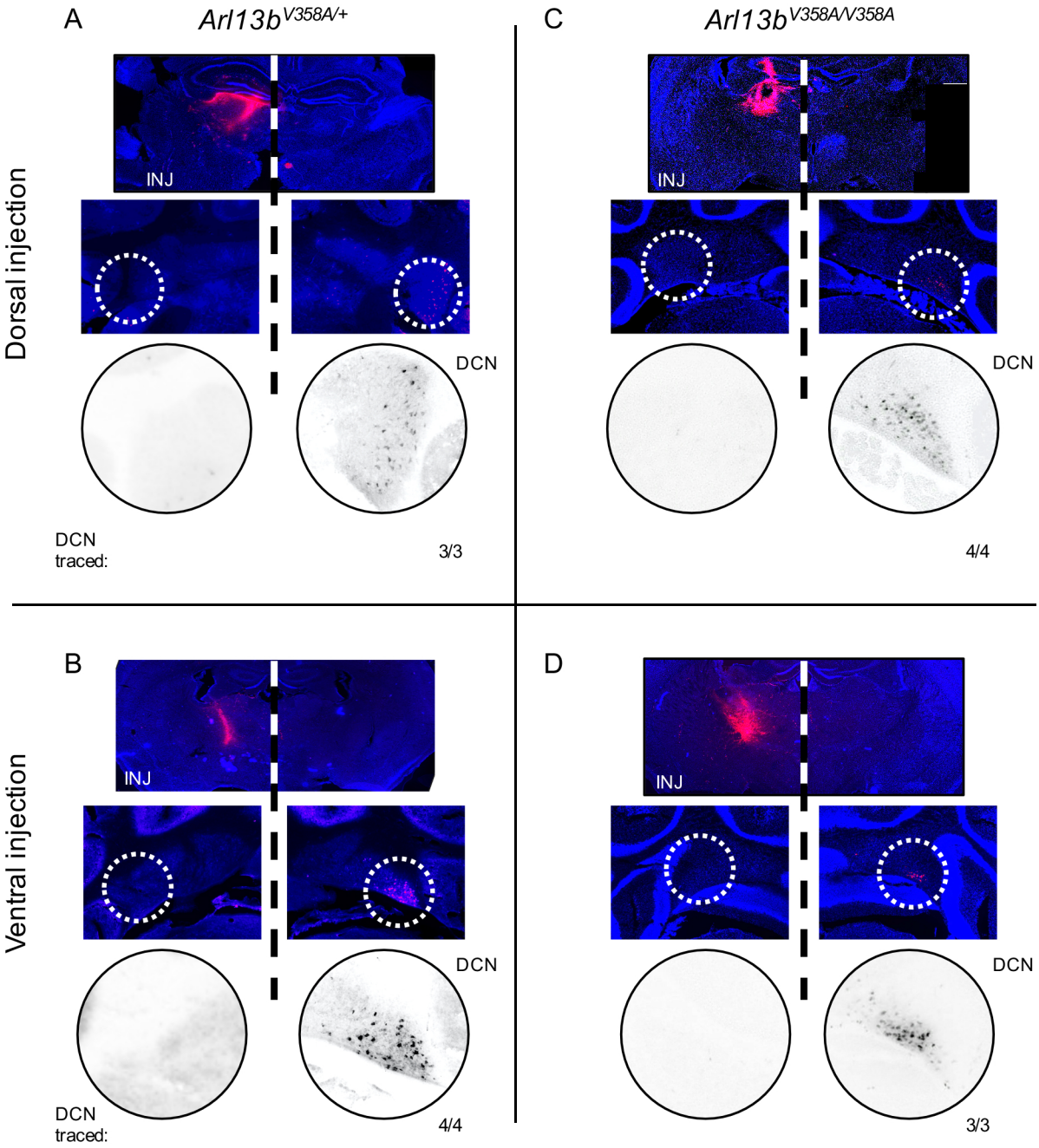
A
Arl13b V358A/+
C
Arl13b V358A/V358A
Dorsal injection
INJ
INJ
DCN
DCN
DCN
traced:
3/3
4/4
B
D
Ventral injection
INJ
INJ
DCN
DCN
DCN
traced:
4/4
3/3

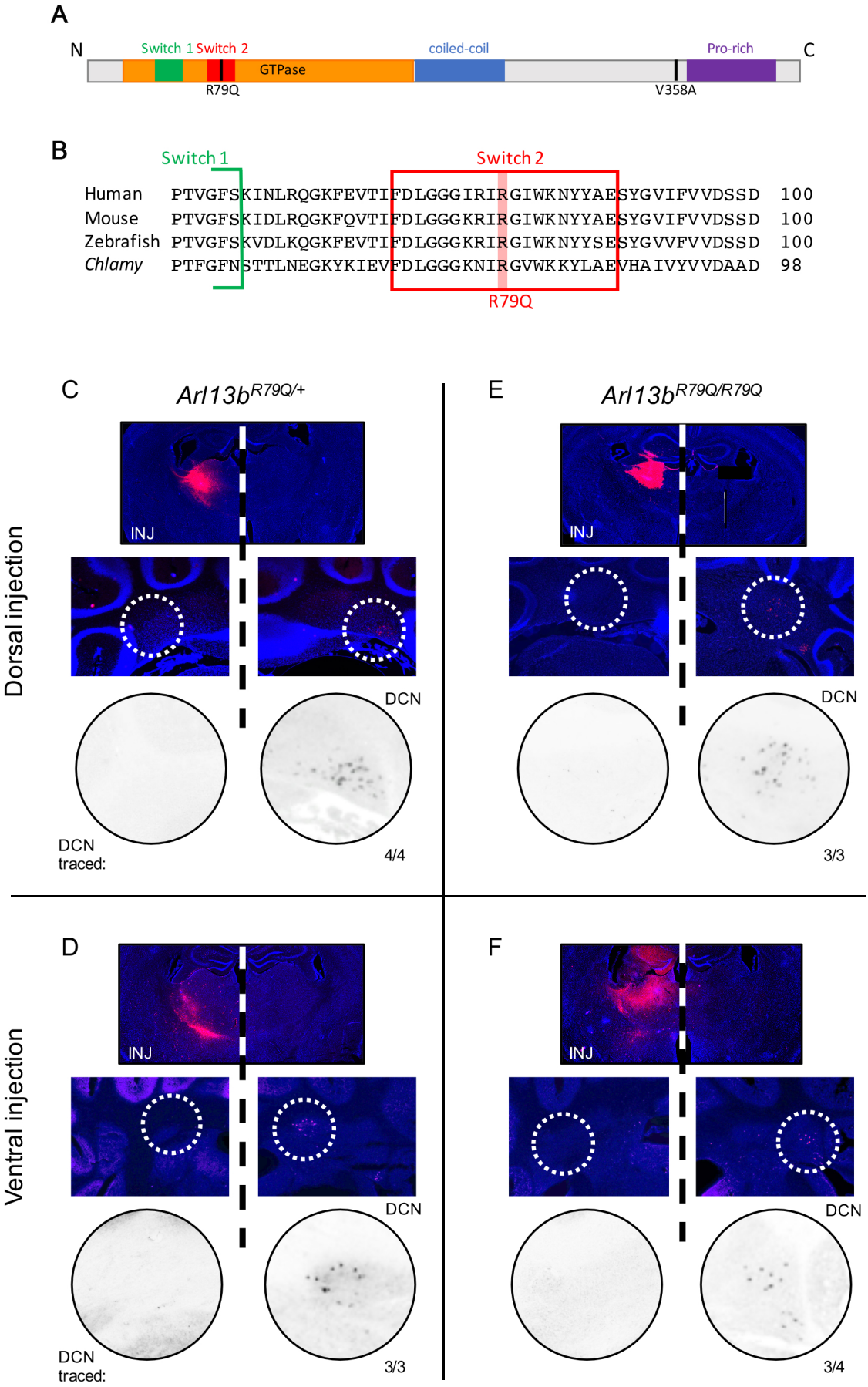
A
N
Switch 1
Switch 2
GTPase
coiled-coil
Pro-rich
C
R79Q
V358A
B
Switch 1
Switch 2
Human PTVGFSKINLRQGKFEVTIFDLGGGIRIRGIWKNYYAESYGVIFVVDSSD 100
Mouse PTVGFSKIDLRQGKFQVTIFDLGGGKRIRGIWKNYYAESYGVIFVVDSSD 100
Zebrafish PTVGFSKVDLKQGKFEVTIFDLGGGKRIRGIWKNYYSESYGVVFVVDSSD 100
Chlamy PTFGFNSTTLNEGKYKIEVFDLGGGKNIRGVWKKYLAEVHAIVYVVDAAD 98
R79Q
C
Arl13b R79Q/+
E
Arl13b R79Q/R79Q
Dorsal injection
INJ
DCN
DCN traced:
4/4
3/3
D
F
Ventral injection
3/3
3/4

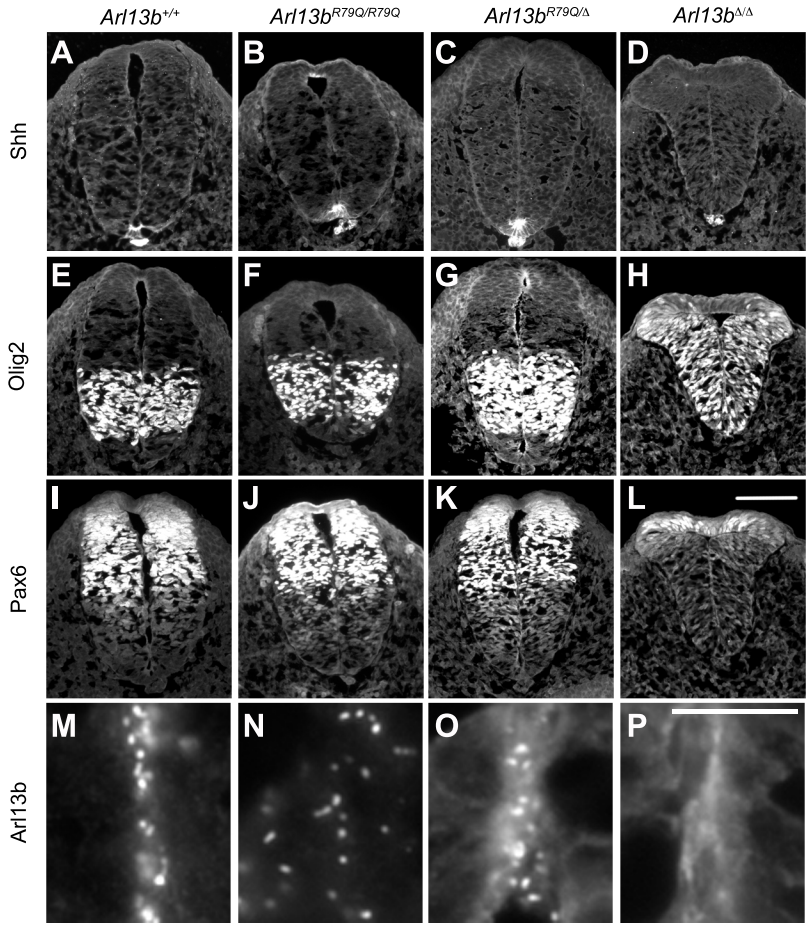
Arl13b+/+
Arl13bR79Q/R79Q
Arl13bR79Q/Δ
Arl13bΔ/Δ
Shh
Olig2
Pax6
Arl13b
A
B
C
D
E
F
G
H
I
J
K
L
M
N
O
P

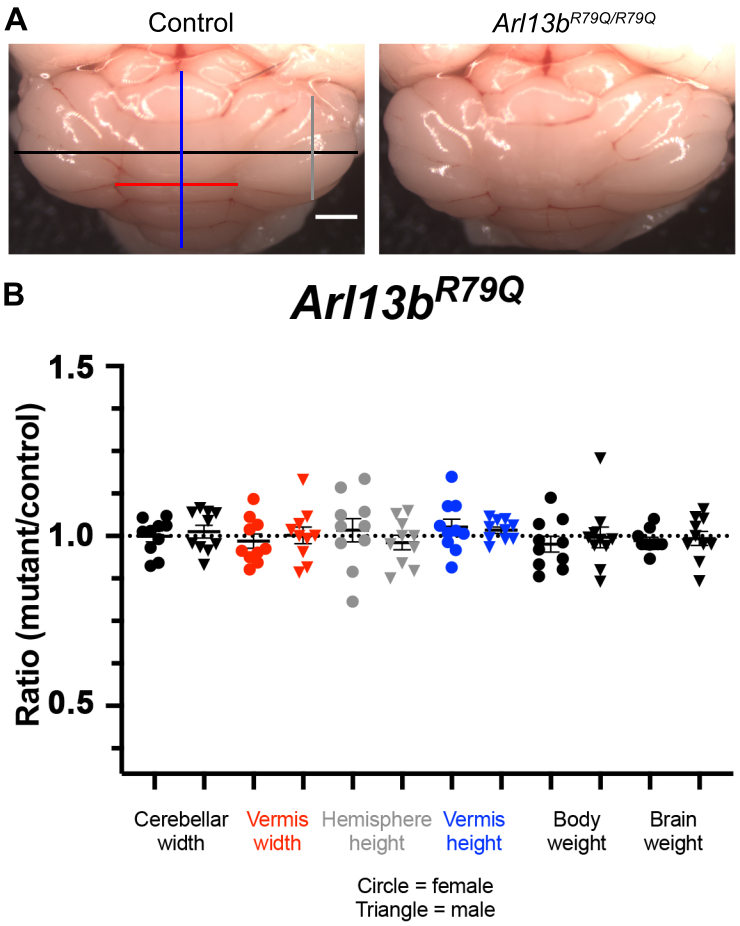
A
Control
Arl13b R79Q/R79Q
B
Arl13b R79Q
Ratio (mutant/control)
1.5
1.0
0.5
Cerebellar width
Vermis width
Hemisphere height
Vermis height
Body weight
Brain weight
Circle = female
Triangle = male

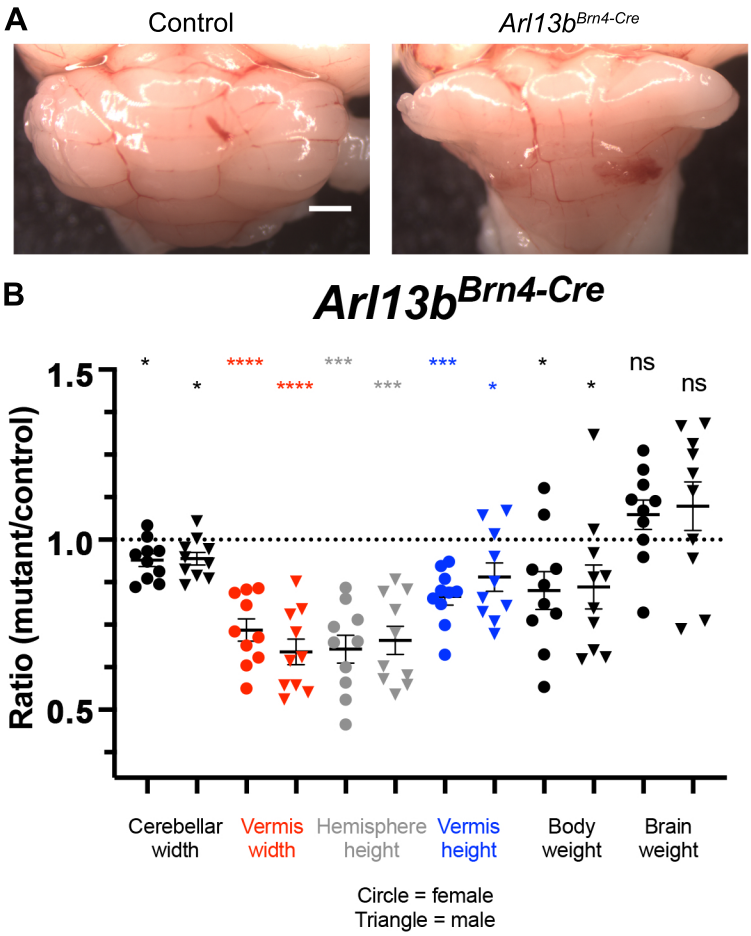
A
Control
Arl13b Brn4-Cre
B
Arl13b Brn4-Cre
Ratio (mutant/control)
1.5
1.0
0.5
*
*
****
****
***
***
***
*
*
*
ns
ns
Cerebellar width
Vermis width
Hemisphere height
Vermis height
Body weight
Brain weight
Circle = female
Triangle = male

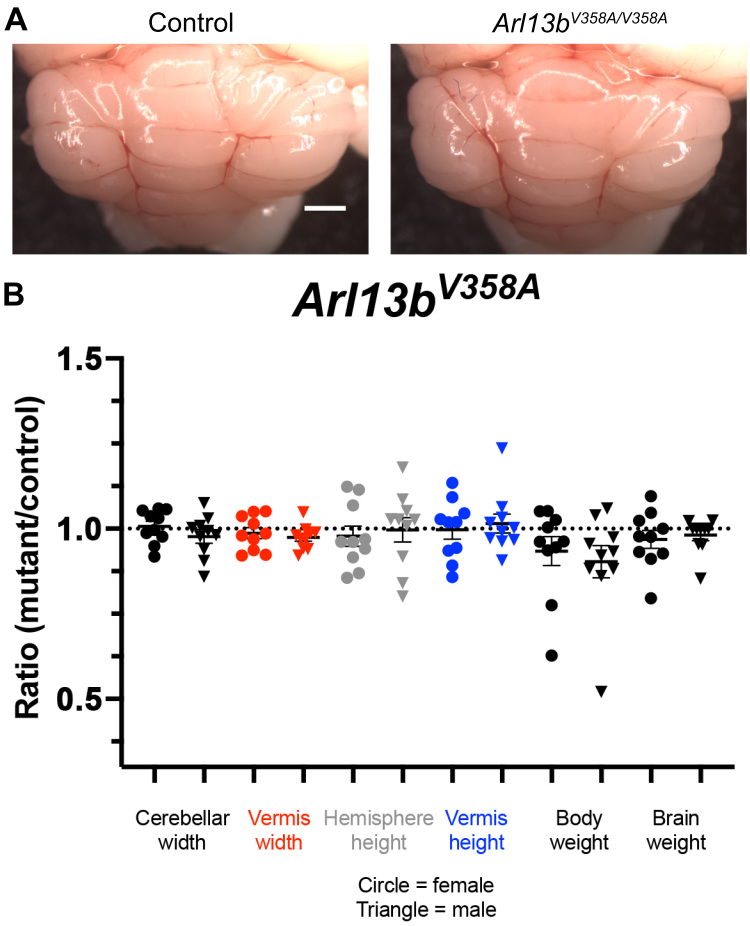
A
Control
Arl13b V358A/V358A
B
Arl13b V358A
Ratio (mutant/control)
1.5
1.0
0.5
Cerebellar width
Vermis width
Hemisphere height
Vermis height
Body weight
Brain weight
Circle = female
Triangle = male